UNIVERSIDAD TECNICA FEDERICO SANTA MARIA
DEPARTAMENTO DE INGENIERIA METALURGICA
Y DE MATERIALES

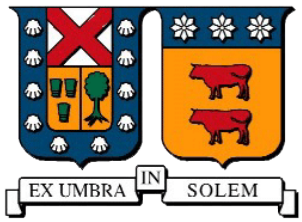

UNIVERSIDAD TECNICA
FEDERICO SANTA MARIA

ANÁLISIS DEL CRECIMIENTO DE GRIETA EN FATIGA EN TORNO AL ΔK_{th} Y DEL FENÓMENO DE CIERRE DE GRIETAS PARA LAS SERIES DE FUNDICIÓN DÚCTIL: 400-15, 500-7, 600-3 Y 700-2

Trabajo de titulación presentado en conformidad a los requisitos y reglamentos requeridos para obtener el título de Ingeniero Civil Metalúrgico

Profesora Guía : Dra. Jessica Elfsberg
Profesora Patrocinadora DIMM: Dra. Karem Tello Araya

EDGARDO MAXIMILIANO CABEZA ESPINOZA

2022

UNIVERSIDAD TECNICA FEDERICO SANTA MARIA
DEPARTAMENTO DE INGENIERIA METALURGICA
Y DE MATERIALES

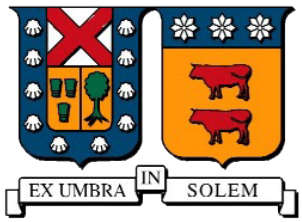

UNIVERSIDAD TECNICA
FEDERICO SANTA MARIA

ANALYSIS OF FATIGUE CRACK GROWTH NEAR THE THRESHOLD ΔK_{th} AND CRACK CLOSURE PHENOMENON FOR DIFFERENT DUCTILE CAST IRON SERIES: 400-15, 500-7, 600-3 & 700-2

Trabajo de titulación presentado en conformidad a los requisitos y reglamentos requeridos para obtener el título de Ingeniero Civil Metalúrgico

Advisor 1: Dra. Jessica Elfsberg
Advisor 2: Dra. Karem Tello Araya

EDGARDO MAXIMILIANO CABEZA ESPINOZA

2022

ABSTRACT

Ductile Cast Iron (DCI) with ferritic to pearlitic matrices are used in a wide range of applications. In a heavy-duty truck the material group is selected for parts exposed to cyclic loads potentially leading to fatigue fractures. For fatigue crack growth (FCG) the stress intensity threshold value for crack propagation, ΔK_{th}, is the parameter to consider.

To have a better understanding of the DCI series EN-GJS-400-15, EN-GJS-500-7, EN-GJS-600-3 and EN-GJS-700-2, the company SCANIA encouraged this research to determine experimentally such threshold value for fatigue crack propagation at different stress load ratios R. In addition, the crack closure phenomenon and its impact on the $\Delta K_{th,eff}$ are analyzed, since there is scarce information regarding their quantitative influence and the main mechanisms present in DCI's.

It was found that the four series shared similar FCG parameters and crack propagation patterns. ΔK_{th} was around 12, 10 and 6 MPa$\sqrt{m}$ for R = 0,1; 0,4 and 0,7 respectively. Their cracking patterns were mixed between inter and transgranular fracture, no matter the pearlite-ferrite content in the matrix. Branching was also found in most of the specimens, even at their crack tips.

Graphite nodules played a fundamental role as crack growth arrester mechanism, since cracks propagated mostly around them, causing a deflection on its direction and, therefore, an increase of the fracture surface roughness. This is directly related with the crack closure due to the friction of such surfaces that hinders the crack opening.

Consequently, there was a gap between the fatigue thresholds that showed up at R lower than 0,7, since $\Delta K_{th,eff}$ values were about 10, 9 and 6 MPa$\sqrt{m}$ for R = 0,1; 0,4 and 0,7 respectively. Energy-dispersive X-ray Spectroscopy (EDS) on the fractured surfaces confirmed friction produced by the crack closure, since there was a high content of oxygen as a product of fretting corrosion for those samples tested at R=0,1 and 0,4, while it was practically absent at R=0,7.

TABLE OF CONTENTS

1. INTRODUCTION

1.1. Context

The production of engineering materials in the automotive area must meet safety criteria, such as high rates of impact absorption of the elements that surround a driver and passengers, sufficient mechanical strength of the chassis of a vehicle, as well as possess fatigue and abrasion resistance for those components that wear out either by the combustion in the engine, cyclical loads that tend to suffer due to load swings or the overuse in some elements like axles, brakes, clutches, among others [1].

Achieving those safety criteria at a reasonably low cost has been of great interest in the world of the motor vehicle and equipment market. Depending on the region or country, standards must be met for a vehicle to be accepted in that market, such as the standards of the UNECE (United Nations Economic Commission for Europe) or those of its American counterpart FMVSS (Federal Motor Vehicle Safety Standards). In turn, these standards have increased their demands considering the experience acquired over time. Therefore, continuous improvement standards have been developed for industries, among which the standard IATF 16949 highlights globally [2].

Since 1843 problems related to material fatigue have been studied [3] due to the failure of the shaft in one of the engines of a transport train in England that caused 70 fatalities. In a time prior to that estimated, and without previous notice, the shaft fractured within the stress tolerance margins of that time, without prior awareness of the effect of fatigue on the materials.

The company SCANIA AB of the Volkswagen group founded in 1900 is one of the leaders in innovation, technology, quality and sustainability in the automotive industry. It stands out in production of cargo trucks, transport buses and engines for heavy machinery, as well as for its operation and maintenance services. Net sales and operating income for 2020 were strongly affected as a result of the pandemic, because if by 2019 sales amounted to over 150 billion SEK (Swedish crowns), they decreased to 125 billion.

Regarding operating income, its reduction in was practically 50%, reaching around SEK 9 billion in 2020 [4]. Its market expands through nearly 100 countries, mainly between Europe, Latin America, Africa, Asia and Oceania. Scania has developed a state-of-the-art concept in the use of both Vermicular and Ductile Cast Iron (DCI), as well as aluminum alloys when required. Therefore, it is in an active search and investigation of materials for the manufacture of its products incorporating continuous improvement in the already established safety criteria.

One of the most used materials in its automotive components are nodular gray cast irons, which are characterized by a simpler production method than steel, being capable of also acquiring high mechanical resistance. They offer the ductility necessary for vehicles to tolerate sudden movements caused by unpaved or defective roads, in addition to the stresses caused by the movement of the load in trucks and transport vehicles. Currently, the grades of greatest interest to SCANIA are EN-GJS-400-15, EN-GJS-500-7, EN-GJS-600-3 and EN-GJS-700-2 according to the standard SS-EN ISO 1563:2018 [5], whose counterparts in the standard ASTM A536 [6] are 60-40-18, 70-50-05, 80-60-03 y 100-70-03, respectively.

1.2. Problem Description

The evolution of materials for the manufacture of vehicles and heavy machinery has placed emphasis mainly on the novelties offered by the varieties of commercial steels, whether they are low-alloy and high-strength, *dual phase*, TWIP (*Twinning Induced Plasticity Steel*), among others [7]. The same happens with aluminum alloys that, being of low density compared to iron, can be used to reduce fuel consumption and, therefore, produce improvements in the efficiency of the final product.

Unfortunately, for the DCI series 400-15, 500-7, 600-3 and 700-2, there has not been entirely conclusive progress in studies related to their mechanical behavior in fatigue, which limits the applications and fields where they can perform. It occurs due to the lack of studies to predict both useful life and tolerance under cyclical stresses, typical of cargo transportation. Although such castings have the required tensile strength, they cannot be

used in more efficient part designs until fatigue is fully incorporated into their safety parameters.

The purpose of this work is to offer to SCANIA designers the appropriate elements to improve and promote the confidence of their products. The study of fatigue through cyclic stresses is of particular interest to SCANIA because these are one of the causes of failure that does not yet have sufficient parameters for the design of its vehicle and heavy machinery components, having to appeal to oversizing. Fatigue Crack Growth (FCG) tests will be aimed to obtain the value ΔK_{th} for each DCI, which indicates the minimum stress intensity factor ΔK from which a crack begins its propagation under cyclic stresses.

Within the same research framework related to fatigue cracking, the *Materials Technology* department at SCANIA requires progress in the study of the crack closure phenomenon and its implication on ΔK_{th} for ductile cast irons. It is still a controversial topic in the scientific community due to the difficulty of contrasting the theoretical with the empirical data, as well as the number of alloys involved and time that each test requires for each of them.

By knowing the behavior of cracks around the threshold value ΔK_{th}, the requirements for the improvement, implementation or replacement of parts can be evaluated in areas where it is convenient to use such DCI, which arose in their time practically by coincidence, but now they can be thought for engineering purpose and sustenance.

1.3. Research Goals

Main Goal:

- Evaluate the threshold value ΔK_{th} of the ductile cast irons of grades 400-15, 500-7, 600-3 and 700-2 to develop a criterion of tolerances for cyclic stresses and defect sizes for SCANIA's purposes

Specific Goals:

1. Generate a database of ΔK_{th} values for the group of DCI given by SCANIA's supplier in the as-cast condition for CT (compact tension) specimens, which are obtained from blocks with 50 and 75 mm thick. Tests are run as described in ASTM E647 standard.

2. Study the behavior of crack propagation through graphite nodules for each DCI with their respective differences in matrix composition, varying the load ratio R and comparing the type of fracture, crack path and roughness of the fractured surface for each material.

3. Analyze the crack closure phenomenon for different stress load ratios (R>0), first qualitatively through microscopic analysis of the corrosion on the contact surfaces and cracking patterns, then quantitatively by the relationship and differences between ΔK_{th} and $\Delta K_{th,eff}$ obtained in the experiments.

4. Evaluate the fatigue cracking tolerance of the target castings using the empirical Kitagawa-Takahashi relationship, thus giving an approach to determine both the acceptable size limits of round defects like porosities, as well as the maximum cyclic stresses that the material can be subjected without cracking.

2. BACKGROUND

2.1. Origin of fatigue cracking in metallic materials

Fatigue cracks in metallic materials in general can be produced by various factors that act cooperatively with the external stress applied by a cyclical load. Factors associated with fatigue cracking include inclusions, soft second phase particles, porosities, surface defects and internal cracks generated during solidification [8], [9].

Although each factor differs in importance regarding the extent to which they affect cracking, they coincide in that they act as concentrators of internal forces in the material. Such forces may give rise to a crack if a cyclical stress greater than or equal to the fatigue limit $\Delta\sigma_e$ is applied. In addition, neither the stress amplitude nor the maximum stress component of the fatigue limit need to be higher than the ultimate tensile strength UTS, since cracking and fracture under fatigue can occur below the yield stress [10].

Griffiths explains the origin of fracture mechanics in fatigue through non-propagating cracks [11], those that stagnate at a given effort, but could potentially spread once the associated energy threshold is exceeded, which is represented by the following equations:

$$G = \frac{\pi\sigma^2 a}{E} \tag{2.1}$$

$$\frac{dG}{da} < \frac{dR}{da} \tag{2.2}$$

$$R = 2\gamma_s \tag{2.3}$$

G corresponds to the energy required for crack propagation, σ is the external stress perpendicular to the crack plane, a is either the half length of an internal crack or the total length of an external crack. E the Young's modulus and R the energy resistance of the

material to crack propagation associated with surface energy γ_s that is empirically obtained for each material due their own microstructure defects [11].

When the system is in equilibrium, the relationship described in equation (2.2) is fulfilled, i.e., there will not be crack propagation if the variation of the energy resistance R is not exceeded in the face of the variation of the length of a crack caused by a stress σ. However, if the stress is higher than the R threshold, it happens that the energy is also greater than the material can withstand, so equation (2.4) is fulfilled and the crack propagation is imminent.

$$\frac{dG}{da} > \frac{dR}{da} \tag{2.4}$$

This propagation causes an increase in the length of the crack that can be stable or unstable, depending on the applied stress and material's properties. Then Irwin [11] complemented it by matching the variables G = R from equations 2.1 and 2.3:

$$\sigma_{critical} = \sqrt{\frac{2E\gamma_s}{\pi a}} \tag{2.5}$$

Equation 2.5 shows that there is a critical stress before which a material is capable of tolerate prior to its energy release that leads to cracking and, therefore, an eventual fracture. Because of this, the concept of stress intensity factor *K* has been developed, whose example equation for the case of an infinite plate can be written as:

$$K_i = \sigma\sqrt{\pi a} \quad ; \, i \in \{I, II, III\} \tag{2.6}$$

$$K_{Ic} = \sigma\sqrt{\pi a_c} \tag{2.7}$$

K_I represents the stress intensity factor *K* in mode I, i.e., stresses are perpendicular to the crack plane and similarly for $i = II$ and $i = III$, depending on whether the stresses are shear parallel to the crack plane or towards the sides respectively. K_{Ic} is the parameter that indicates the fracture toughness for monotonic loads. This parameter indicates the material resistance to cracking prior to fracture, being subjected only to increasing stresses from resting state.

As described by equation 2.7, K_{Ic} depends both on the stress to which it is subjected and on the size of the previous crack in question, maintaining an equilibrium such that, the larger the critical crack size a_c, the lower the stress tolerated against fracture.

On the other hand, as well as there is a fracture toughness parameter, in the study of fatigue cracking of materials it is possible to determine the threshold value ΔK_{th} before cyclical loads, that is, with loading and unloading cycles. Hence, there is a stress range $\Delta\sigma$ related to the amplitude given by the maximum and minimum load given by the ratio R, as shown in equations 2.8 and 2.9.

$$\Delta K_{th} = \Delta\sigma\sqrt{\pi a} \tag{2.8}$$

$$R = \frac{P_{min}}{P_{max}} = \frac{K_{min}}{K_{max}} = \frac{\sigma_{min}}{\sigma_{max}} \tag{2.9}$$

To be more precise, ΔK_{th} corresponds to the minimum value of the amplitude *K* before a crack starts to propagate, which considers growth rates up to 10^{-7} mm/cycle from any defect or pre-existing crack [12], [13], thus delimiting the threshold from a crack that does not propagates to one that does.

Each formula related to the *K* factor shown so far is simplified for the geometry of an infinite plate, nevertheless, to limit it to finite dimensions, it is necessary to apply a geometric factor depending on the specimen shape. The methodology section will detail the respective equation to use for the fatigue crack growth (FCG) tests.

2.2. Understanding, application and evaluation of the FCG parameters

The stress intensity factor *K* is defined as a parameter that describes the intensity of the stress field in the vicinity of the tip of a crack. Such stresses can be produced either by monotonic or cyclic loads, the difference of which lies in the fracture mechanisms due to a high singular stress, or to a high number of loads at lower stress levels.

While the K_{Ic} is the fracture toughness index of a material subjected to monotonic loads, ΔK_{th} corresponds to the threshold value of the amplitude of the stress intensity factor that the material tolerates in fatigue prior crack propagation. The basis for obtaining and applying such threshold is that the material has a predominantly linear elastic behavior, so that there is not significant plastic deformation in the contour of the crack tip [11].

One way to analyze and understand the K_{Ic} and ΔK_{th} is through Figure 1 that shows a schematic graph of FCG. It illustrates the behavior of a crack as a function of ΔK and crack growth rate for each load cycle (da/dN). It is observed that the curve of the graph is divided into three regions, which implies that the crack of a material has different behaviors depending on the magnitude ΔK.

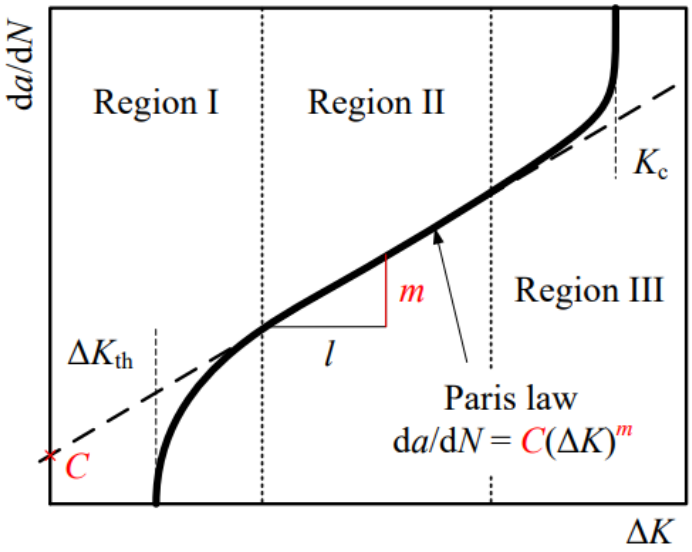

Figure 1 Typical Fatigue Crack Growth for a metallic material [14].

For stress amplitudes greater than the threshold value ΔK_{th}, the first region shows how the crack begins to propagate. Then, if the ΔK continues to increase, the crack tends to grow stably according to the intrinsic factors C and m (given by the slope) of the material in question, so it would behave according to the Paris Law throughout the second region. Finally, if the ΔK continues to increase towards values close to the K_{Ic}, the crack stops obeying the Paris Law and begins to grow unstably until an imminent fracture.

As defined before, ΔK_{th} is the threshold value of ΔK at which the crack growth is barely higher than zero. It is empirically determined by FCG tests at crack propagation rates from 10^{-6} to 10^{-7} mm/cycle, whose procedure is described by ASTM E647 [12] and ISO 12108 [13]. On the other hand, K_{Ic} is the point value from which a crack grows in an unstable way, a value to which no material is expected to reach during its useful life, since it is the critical fracture indicator whose official standard is ASTM E399 [15].

Another way of evaluating the aforementioned parameters is by means of the empirical relationship developed by Kitagawa and Takahashi [16], [17] as shown in Figure 2 , which relates the crack size, a, as a function of the applied cyclic stress $\Delta\sigma$. The inner region corresponds to the safety zone were, at most, there will only be cracks incapable of propagating. The top limit is given by the fatigue limit $\Delta\sigma_e$, while the side limit is plotted according to the equation for $\Delta\sigma$ shown in the same figure, expressed in terms of a, ΔK_{th} and the crack shape factor “y”.

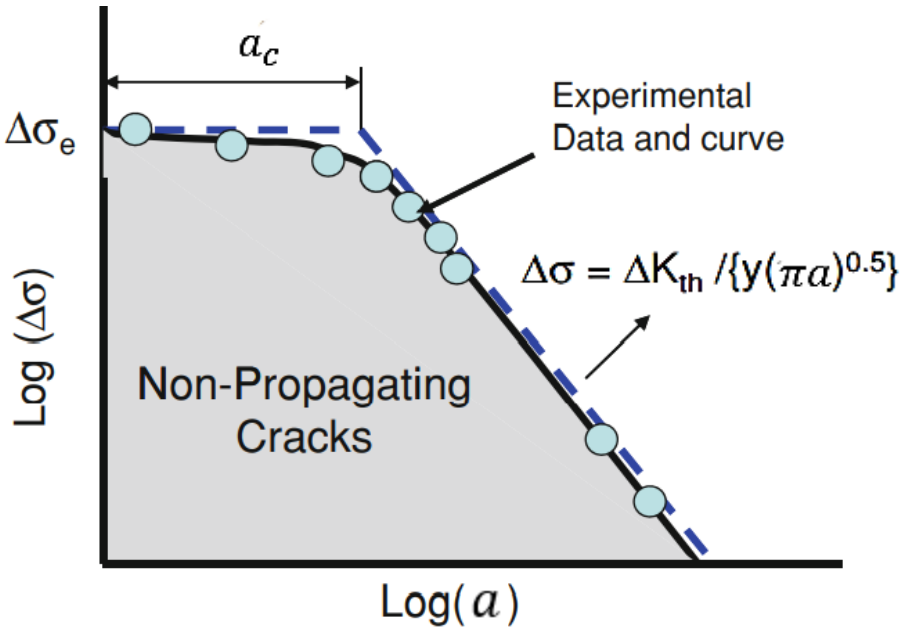

Figure 2 Schematic Kitagawa - Takahashi diagram [17].

All materials are expected to be within the safe zone throughout their useful life, since if the stress $\Delta\sigma_e$ is exceeded, crack propagation may begin. If this were the case, the part in question would be susceptible to an eventual fracture, since, if the cyclic loads remain the same as the crack grows, the stress intensity factor would increase indefinitely, being able to fail at time to reach K_{Ic}.

Moreover, if loads $\Delta\sigma = \Delta\sigma_e$ are applied on a metallic material with a crack of critical size a_c, it will fracture instantaneously, since the applied K value would coincide with the K_{Ic}. Therefore, in practice, the security zone has a curvature around these coordinates, which was empirically proven by El-Haddad [16].

2.3. Influence of crack closure phenomenon and stress load ratio R on ΔK_{th}

The crack closure phenomenon dates its research back to 1970, when Elber studied the behavior of cracks under cyclic stresses [18]. He realized for the first time about the unconformity between the Crack Mouth Opening Displacement (CMOD) and the applied load along its opening.

Elber evidenced the change in compliance corresponding to the intrinsic value of each material that denotes its flexibility, represented by the variation in elongation per unit of applied force, whose measurement can be given in m/N. Figure 3 describes the aforementioned relationship, where it can be seen that for closed cracks the change in displacement with respect to the applied load is less compared to that of an open crack, implying that one does not behave in the same way throughout the charge and discharge cycle.

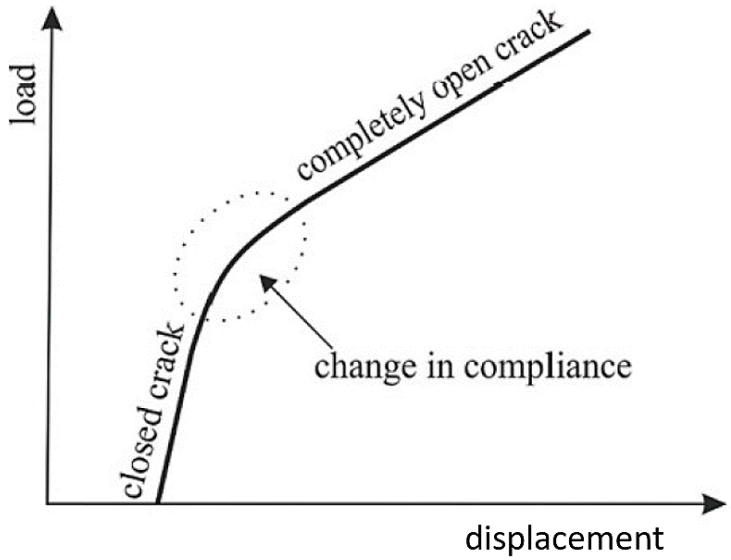

Figure 3 Compliance variation for a crack in closed and open status [19].

This phenomenon refers to different factors, among which corrosion by oxidation, surface roughness, dirt and Plasticity Induced Crack Closure (PICC) stand out, which can affect individually or jointly on the surfaces in contact of a crack [11], [19], [20] in such a way that the propagation of the crack tends to stagnate.

With regard to ductile cast iron, the original cause of the crack closure phenomenon is the PICC [21], which consists of the plastic deformation around the tip of the crack that advances parallel to the propagation, as observed in Figure 4: (a) shows the general pattern of advance and change of orientation of the dislocations, (b) and (c) describe the orientation at the level of crystalline lattices around the contact surfaces of the crack and (d) exemplify the cases with and without deformation restrictions, since if there were no stiffness in the contour, the CMOD would increase along with the crack propagation.

Although PICC has an impact only at a microscopic level, it is enough to produce a mismatch between the fractured surfaces that causes friction in between. Besides, because of crack deflection proper of heterogeneous materials, the effect of roughness induced crack closure becomes more relevant [22], [23].

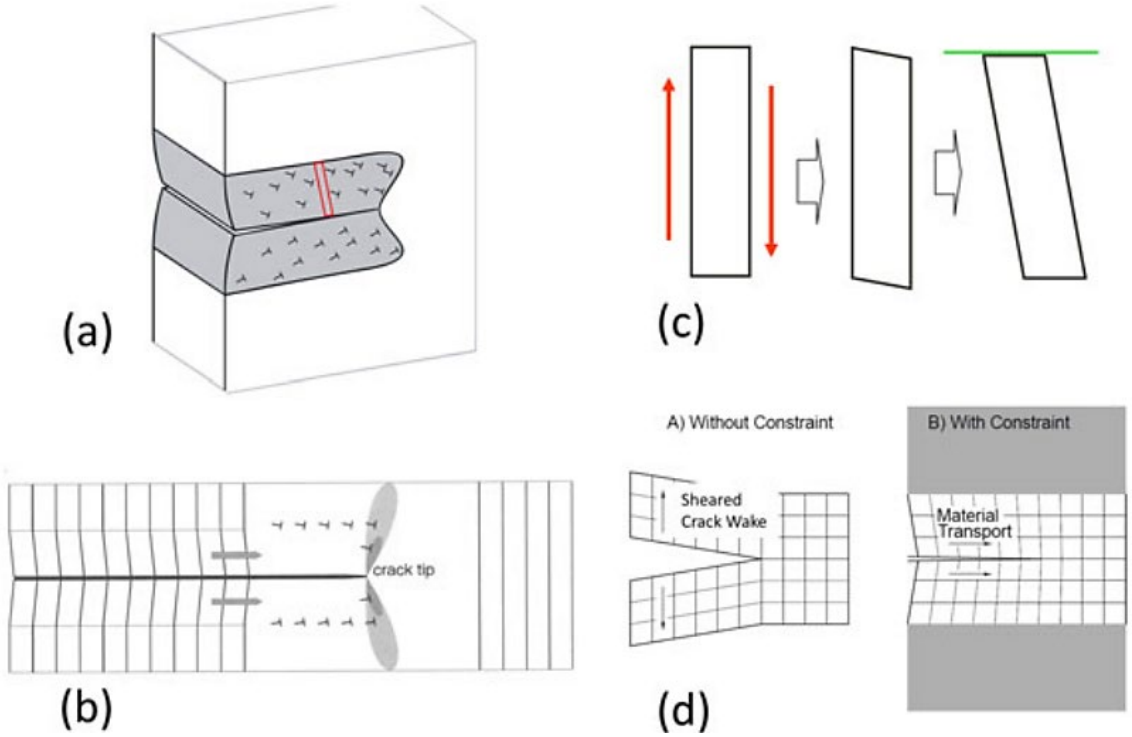

Figure 4 Representation of Plasticity Induced Crack Closure through dislocation displacement and lattice distortion [20]

Since Elber's finding, a variety of studies related to crack closure have emerged over time [27–29], mostly sharing arguments regarding the effect that this phenomenon has on the final value of ΔK_{th}. To understand this quantitatively, it is necessary to resort to the effective stress intensity factor amplitude ΔK_{eff}, whose formulation arises analogously to ΔK according to the following equations:

$$\Delta K = K_{max} - K_{min} \tag{2.14}$$

$$\Delta K_{eff} = K_{max} - K_{op} \tag{2.15}$$

Even though in equation 2.14 the K_{min} is established as a function of the load ratio R, for the case of equation 2.15, K_{op} corresponds to the stress intensity factor necessary for the crack to be completely open, also associated with a load P_{op} . For values of R less than 0,7, it has been determined that it is generally true that $K_{op} > K_{min}$and at the same time $\Delta K > \Delta K_{eff}$, since this phenomenon is present until then.

Therefore, it is possible to determine $\Delta K_{th,eff}$ excluding the crack closure effects through an adjustment in the compliance variation. Figure 5 shows the behavior of K over time, with $\Delta K = \Delta K_{th}$ and a stress load ratio R = 0, whose K_{min} is zero. $\Delta K_{th,eff}$ is obtained from K_{min} = K_{op} to the maximum amplitude K_{max}.

The difference between both thresholds is determined by R, and their gap can be decreased if it gets closer to R*. Hence, R* corresponds to the stress load ratio at which the crack always remains open. $\Delta K_{th,eff}$ would be equivalent to ΔK_{th} only if the load ratio were greater than or equal to R*, where $K_{min} \geq K_{op}$.

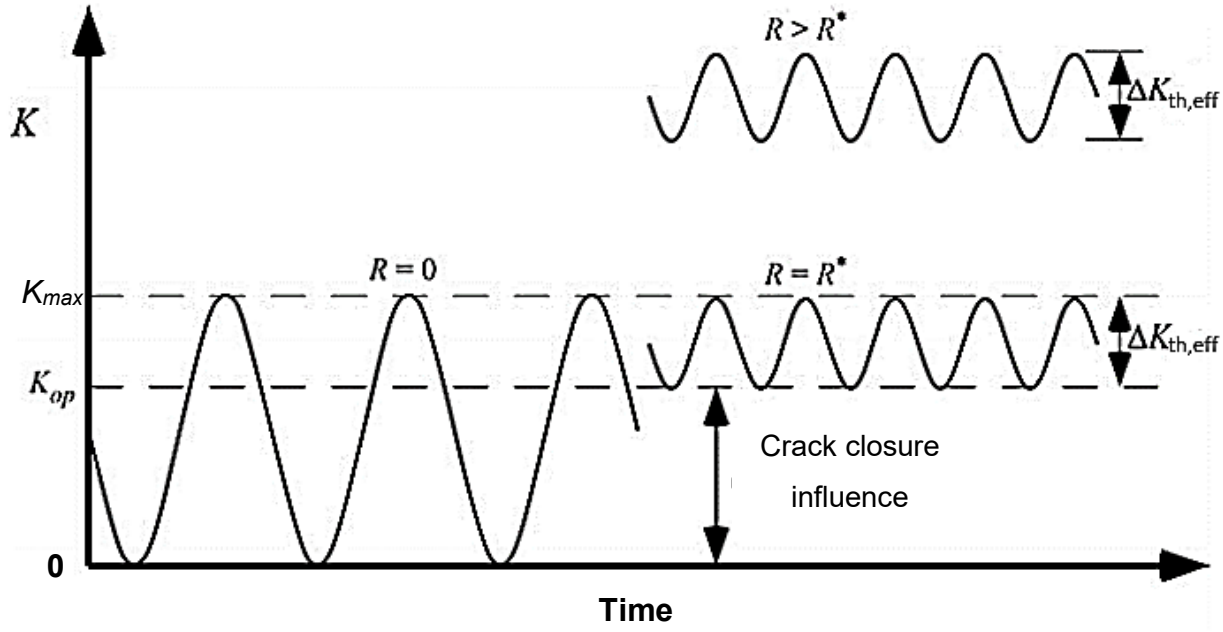

Figure 5 Schematic representation of $\Delta K_{th,eff}$ within ΔK at R=0 [11]

Given the influence of R on ΔK_{th} product of crack closure, it is necessary for researchers to determine the R most appropriate to their study objective. Figure 6 shows schematically how the value of ΔK_{th} decreases as a function of R to R *, then it remains constant since $P_{min} = P_{op}$ and, therefore, $K_{min} = K_{op}$.

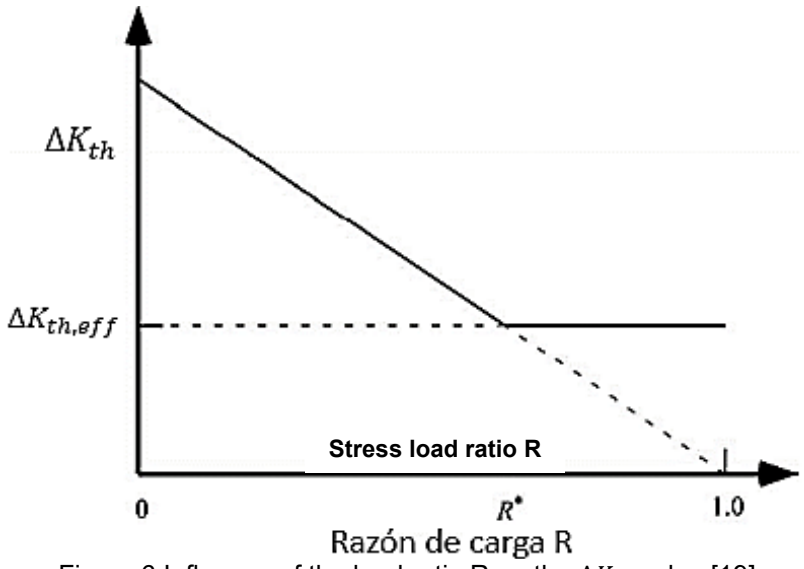

Figure 6 Influence of the load ratio R on the ΔK_{th} value [19].

This phenomenon does not only cause modifications around the threshold value, but also throughout the entire propagation of the crack, being able to affect both the K_{Ic} and the Paris Law parameters at the second region. Figure 7 schematizes the displacement of the propagation curve, where for an R = 0.5 or greater (sometimes with R > 0.7 depending on the material) the modification is minimized [25].

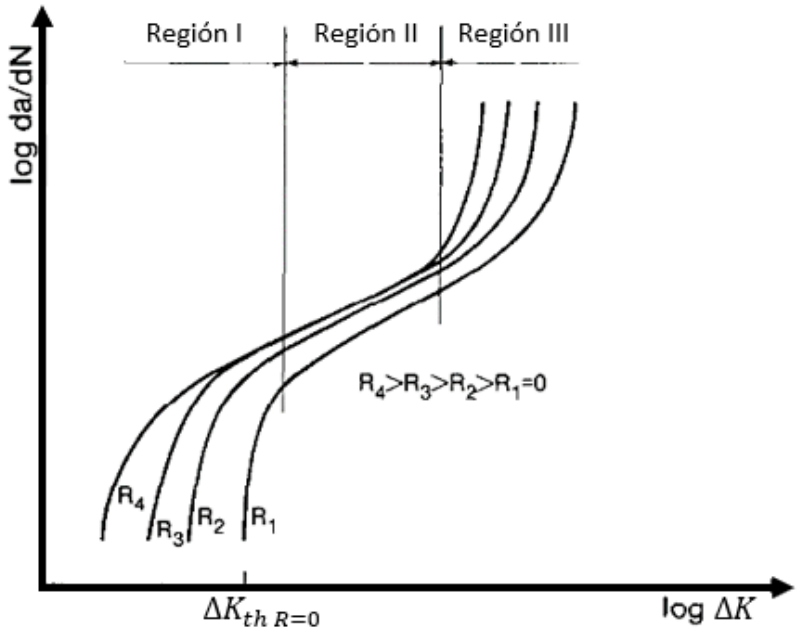

Figure 7 Displacement of FCG curves for different R > 0 [25].

3. MATERIAL DESCRIPTION

3.1. Microstructure, mechanical properties and chemical composition

According to the SS-EN ISO 1563: 2018 [5] standard, ductile cast irons must meet the minimum requirements regarding their tensile properties, for which it is usually required at least 80% nodularity. The nodules are mainly of type V and VI according to ISO 945-1 [26], as shown in Figure 8 and in the micrographs in the APPENDIX C for the studied DCI series.

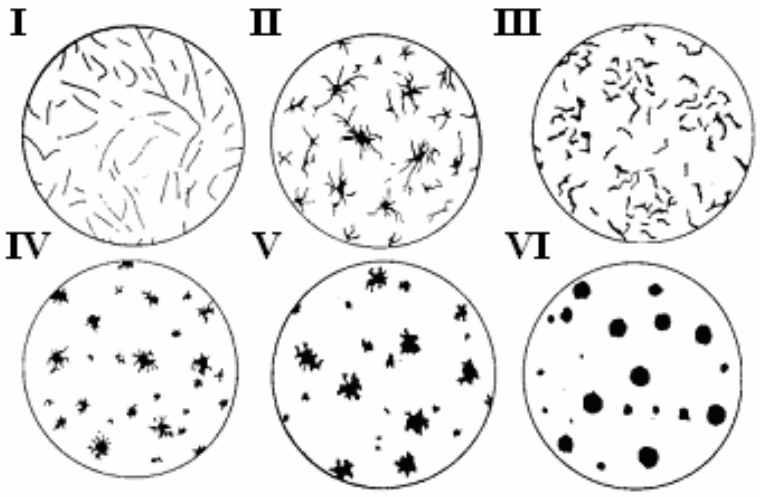

Figure 8. Classification of graphite types for cast iron according to ISO 945-1 [26].

However, there is between 15 to 20% of graphite that does not reach the respective nodularity, then acquiring forms of type IV, rarely type III and even type I and II in some thick pieces, depending on the cooling conditions and distance from mold, among others.

Regarding to the DCI worked in this study, a graphite analysis was done for each series considering only C type samples, shape and class distribution are shown in Figure 43 and Figure 44 respectively from APPENDIX C. There were no big differences in graphite features between structure coarseness to report for A and B samples, as seen on the microstructure overviews in the APPENDIX B. Besides, it is known that there could exist some differences between the center and the outer side of the simples, due to solidification time variations and, therefore, extent diffusion of carbon to the graphite

particles [27], nevertheless, all samples were machined and the graphite analysis was done through the whole cross section.

The matrix is key to differentiate the potential offered by each cast iron with respect to the ferrite and pearlite fractions. The matrix directly affects the mechanical properties as shown in Table 1 and whose composition overviews can be seen in the micrographs of APPENDIX B. As the percentage of pearlite increases, so does the yield point, UTS and $\Delta\sigma_e$, while the ductility decreases with the reduction of ferrite. The chemical composition is detailed in Table 2.

Table 1 Mechanical properties of DCI series 400-15, 500-7, 600-3 and 700-2 according to SS-EN 1563:2018 [5]

DCI	*Thickness t [mm]*	*Yield Strength [MPa]*	*UTS [MPa]*	*Elongation %*	*Matrix composition*	*Fatigue limit $\Delta\sigma_e$ [MPa]*
400–15	***60 ≤ t ≤ 200***	***250***	***400***	***15***	***< 10% Pearlite***	***235***
500–7	***60 ≤ t ≤ 200***	***320***	***500***	***7***	***10-50% Pearlite***	***280***
600–3	***60 ≤ t ≤ 200***	***370***	***600***	***3***	***> 50% Pearlite***	***319***
700–2	***60 ≤ t ≤ 200***	***420***	***700***	***2***	***> 70% Pearlite***	***353***

Table 2 Chemical composition of DCI series studied at SCANIA

Series	***%C***	***%Si***	***%Mn***	***%P***	***%S***	***%Cr***	***%Ni***	***%Cu***	***%Sn***
400	3,68	2,39	0,21	0,03	0,02	0,02	0,03	0,05	0,01
500	3,67	2,88	0,77	0,02	0,02	0,12	0,09	0,15	0,01
600	3,60	3,09	0,81	0,02	0,02	0,11	0,09	0,26	0,14
700	3,56	2,85	0,82	0,02	0,02	0,10	0,08	0,93	0,01

3.2. Specimen geometries and orientation

Four ductile cast iron (DCI) grades were tested. They were ordered from an external supplier, and fulfil the requirements for, EN-GJS-400-15, EN-GJS-500-7, EN-GJS-600-3 and EN-GJS-700-2 according to the standard SS-EN ISO 1563:2018.

The tests were performed on compact tension (CT) Specimen for Fatigue Crack as described in ASTM E647, whose dimensions are illustrated in Figure 9, with a Straight Through Notch. All the measurements are given in mm and a(n) corresponds to the notch length = 12,5 mm considered for the pre-crack. The CT samples were cut off from the bottom of the Y-blocks, as shown by the hatched region in Figure 10. The iron alloys were sand cast in two Y-block types called III and IV, whose main differences are given by their thickness “u” 50 mm and 75 mm respectively.

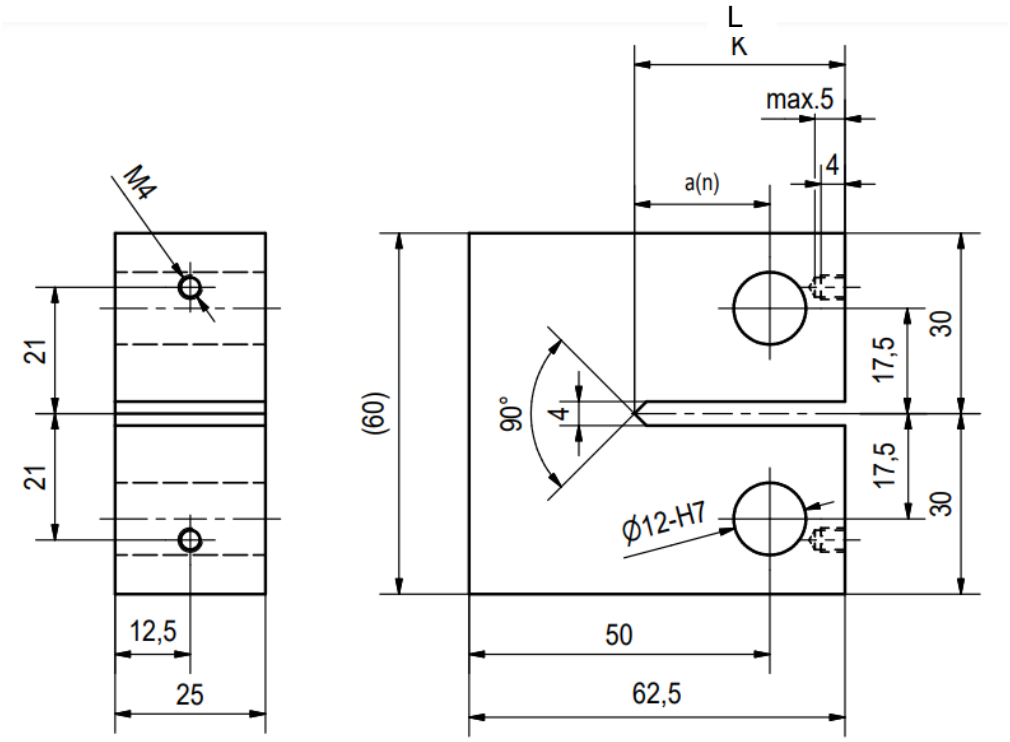

Figure 9: Dimension in mm of compact tension (CT) specimens tested at SCANIA according to ASTM E647 [12].

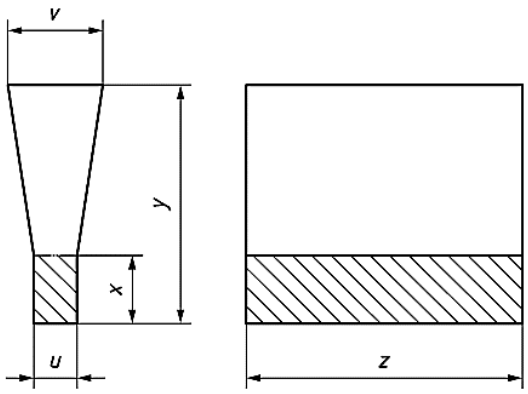

Figure 10 Y-block scheme for sample cutting according SS-EN ISO 1563:2018 [5]

To get the individual CT specimen, the tapered feeder part was cut off. From the sound material of each type III Y-block, three samples were obtained. They all have the same orientation as illustrated in Figure 11a, where the cut off tapered feeder volume was placed above the cross-section shown in the same Figure. Four samples were obtained from Y-block type IV. Their orientation is shown in Figure 11b.

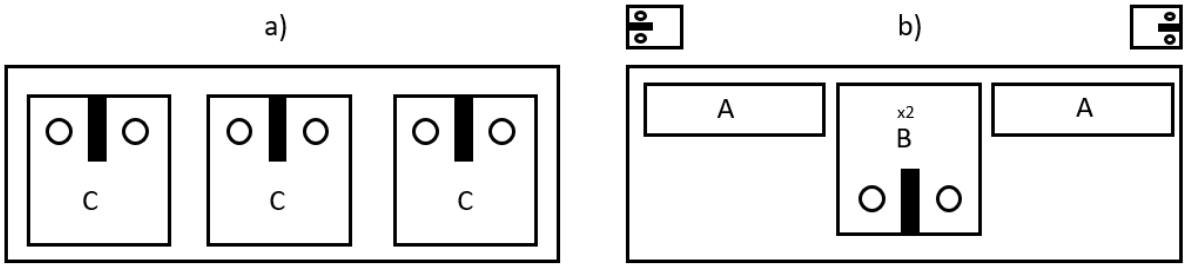

Figure 11 Orientation of the samples in the sound part of respective Y-block. a) Y-block type III, feeder coming from the top. b) Y-block type IV, feeder coming from the behind, i.e., from the plane of the paper.

4. METHODOLOGY

4.1. Fatigue crack growth tests: Compliance method and ΔK calculation for the creation of a database

All the tests were run according to the standard ASTM-E647. The equipment used in this fatigue crack growth experiment was the resonant testing machine Rumul Testronic 150 kN whose load cell for fatigue crack growth reaches up to 20 kN. The frequency was between 70 to 90 Hz.

To apply the compliance method, the extensometer is adjusted in position V_0 according to Figure 12. According to the ASTM E647 standard, the crack length a is determined according to the following equations:

$$a = \frac{\mathrm{a}}{W} = C_0 + C_1 u_x + C_2 u_x^2 + C_3 u_x^3 + C_4 u_x^4 + C_5 u_x^5 \tag{4.1}$$

$$u_x = \left(\left(\frac{EvB}{P} \right)^{\frac{1}{2}} + 1 \right)^{-1} \tag{4.2}$$

Where v corresponds to the opening measured by the extensometer at the front of the crack (CMOD), *P* is the load applied by the machine, C_i are constant parameters given by the standard, E is the Young's modulus and B is the thickness of the specimen.

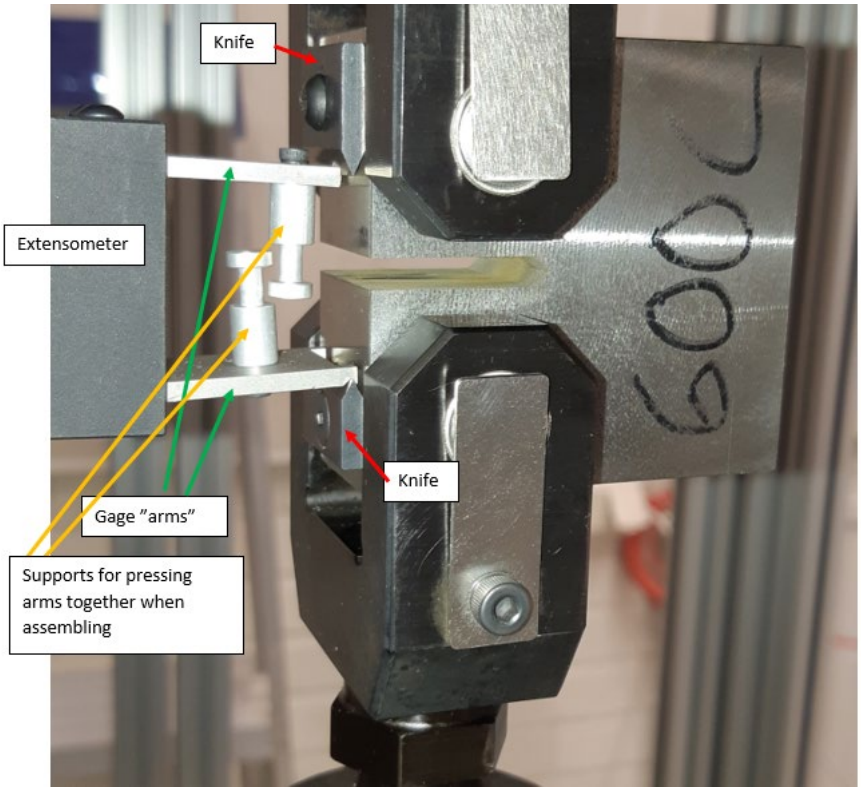

Figure 12 Setup of the sample, extensometer and grips of Rumul's machine.

The machine was configured so that approximately every 1000 cycles it delivers an average ΔK value, which is calculated using equation 4.3, provided by annex A1 of the ASTM E647 standard for the specific case of a CT specimen. Given the above, ΔP and a correspond to average values between each data report.

$$\Delta K = \frac{\Delta P}{B\sqrt{W}} \frac{(2+\alpha)}{(1-\alpha)^{\frac{3}{2}}} (0.886 + 4.64\alpha - 13.32\alpha^2 + 14.72\alpha^3 - 5.6\alpha^4) \quad (4.3)$$

4.1.1. Pre-cracking and tests per sample

Pre-cracking was done under constant stress load ratio R=0.1 and a constant force amplitude. Initially, ΔK was set as high as possible, which was limited by the maximum capacity of the load cell. Then, once the crack started to grow, ΔK increased as well. The number of cycles at the end of the pre-crack ended at 1×10^5 - 2×10^5.

Each sample was pre-cracked from the 12,5 mm crack notch up to 15,5 mm total crack length, with the only exception of 700C2, whose total crack length went up to 18 mm. At least 2 tests per sample were performed applying the K-decreasing method according to ASTM-E647 for da/dN < 10^{-8} m/cycle, so that enough information near the fatigue crack growth threshold (ΔK_{th}) could be acquired as shown in Figure 13.

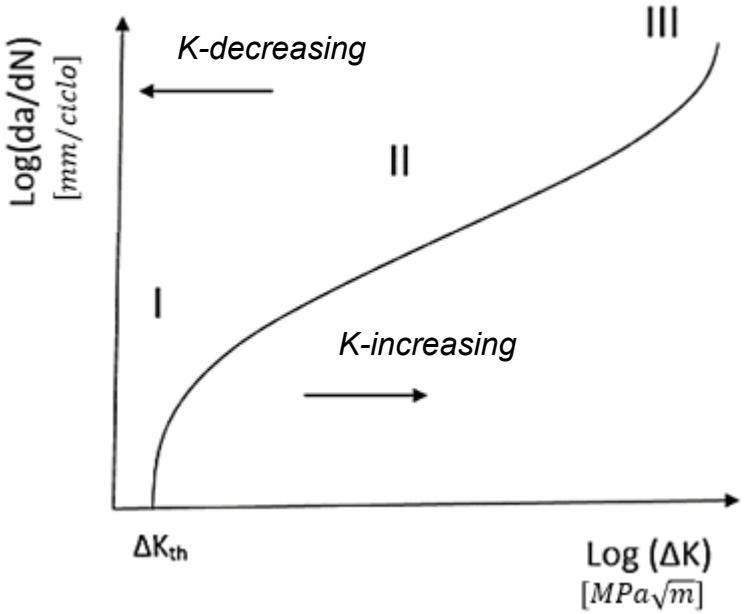

Figure 13 Region of application of the K-increasing and K-decreasing methods in the FCG graph [28].

Once the pre-cracking was done, the first fatigue crack growth (FCG) test started at the highest possible maximum force. To apply the K-decreasing method, the machine module was switched to load control, keeping the R constant while ΔK decreased and K-gradient C = 1/K×dK/da was set to -0,08 mm^{-1}. As ΔK was limited by the load cell capacity, this could not start from the same amplitude for different R, so that the higher the R, the lower initial the ΔK. An example is given in Table 3.

Table 3 Example of initial parameters when doing each test, ΔK in MPa√m.

Sample	***Pre-crack***		***Test 1***		***Test 2***	
	R	**ΔK**	**R**	**ΔK**	**R**	**ΔK**
700C2	0,1	15	0,1	19	0,1	19
700A2	0,1	15	0,4	12	0,7	9

These ΔK values meant crack growth rates of about 10^{-7} - 10^{-8} m/cycle, which made it suitable to proceed with the K-decreasing method. R was kept constant, while force amplitude was switched into decreasing mode to get closer to the threshold.

The second FCG test started after the crack growth rate reached 10^{-9} - 10^{-10} m/cycle, making sure that the crack grew at such speed for at least 0,3 million cycles. If the R to study was the same, then the same initial ΔK was set, but if R was going to be increased, ΔK had to be adjusted so that the maximum force was not exceeded as shown in Table 3.

The stop condition for the second test was controlled by a maximum crack length no larger than 30 mm. In case this condition was not achieved, the test could be stopped manually at any moment once small enough crack growth rates were reached. When possible, the test was left running for a couple of million cycles to make the threshold identification easier.

4.1.2. Stress load ratio R variations

To study both the crack growths in the different materials at different load conditions and the crack closure phenomena, tests were performed at different R values according to Table 4. C2, A1 and B1 series were subjected to R = 0,1 to analyze the potential influence of orientation and coarseness of the microstructure.

On the other hand, B2 series was tested at R = 0,4, whereas A2 series was a mix. R = 0,7 was done every second test because it required enough crack length to reach a crack growth rate of 10^{-10} m/cycle, so, instead of just growing a larger pre-crack, another lower R was used as a first test.

Sample 700 C3 was the one sent to Rumul to compare with the trials C1 done at Scania. Those C3 and B2 samples without a value correspond to spares, in case there was any test wrongly run or for future studies.

Table 4 Sample series and their tested R value

DCI	Test	C2	C3	A1	A2	B1	B2
400	1	0,1	0,4	0,1	0,4	0,1	0,4
	2	0,1	0,7	0,1	0,7	0,1	0,4
500	1	0,1	0,4	0,1	0,1	0,1	0,4
	2	0,1	0,7	0,1	0,7*	0,1	0,4
600	1	0,1	0,4	0,1	0,1	0,1	0,4
	2	0,1	0,7	0,1	0,7	0,1	0,4
700	1	0,1	0,1	0,1	0,4	0,1	0,4
	2	0,1	-	0,1	0,7	0,1	0,7

*Original test 2 for 500 A2 was replaced by a third test, due to lack of data near ΔK_{th}

4.1.3. Calculation of ΔK_{th}, and Paris Law parameters

According to standard ASTM E647-12, ΔK_{th} was calculated in the region where crack growth rate is lower than 10^{-9} m/cycle, using at least five equidistant points of FCG data. C and m parameters were calculated using all data of region II before the apparent slope changes when going to region I.

All the above-mentioned points were worked with their logarithmic values, so that the parameters could be obtained upon a linear regression with a statistical analysis for standard deviation. These calculations were done for each R value and the regarding tests of interest.

4.1.4. Limitations and considerations

All measurements were obtained through the compliance method described in ASTM-E647 and, as shown in equations 4.1 and 4.2, crack length was dependent on load and displacement, so there was always an offset between the initial load that determines the starting crack length without crack propagation, and the load at which the test actually starts. Despite this offset is considered by Rumul's machine, it mostly depends on the user how good this variation is corrected.

As the load cell has a limit of 20 kN, it was not convenient to start the first tests with a high R value such as 0,7 for the present materials, because the crack growth rate was too low and data would be collected only in a very narrow range of ΔK.

Among the possible complications that may arise during fatigue crack growth tests are the curvature of the front of the crack caused by the effect that the SS ISO 12108 standard calls *tunneling* [13], referring to the advance in the form of tunnel through the specimen as shown in Figure 14.

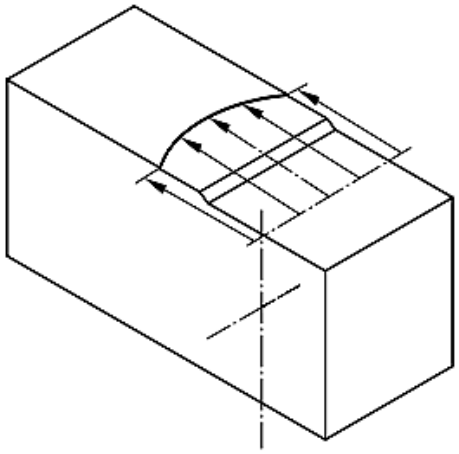

Figure 14 Tunneling effect through the cross section of a CT sample [13].

4.2. Sample analysis: Different approaches to study crack propagation paths and crack closure phenomena

Once the second test was finished, each sample was subjected to one of two possible procedures: 1) cut off the surrounding cracked zone of the CT specimen or 2) break it off under monotonic load.

The first method was done for fatigue crack growth analysis, such as crack tips, branching and path through the microstructure. When the sample was cut, two surfaces were analyzed: the side and the centerline of the cross section.

The second method allowed the study of fracture surface roughness (FSR) and manual measurements of final crack lengths after each test by using a stereo microscope Zeiss Axio Zoom V16. These measurements included the crack front curvature corrections according to the standard ASTM-E647.

4.2.1. Etching

Two different etchants were used depending on the purpose: Nital which is 2% nitric acid in ethanol and a picric acid solution prepared by mixing 100 ml picric acid 2.1% with 25 grs of NaOH pellets.

Nital was used at room temperature for a couple of seconds (usually 5 - 10 s) to reveal pearlitic and ferritic structures. Picric acid solution was used at 90 °C and the sample was immersed for 7 - 8 minutes while the solution was fresh It is recommended to decrease the immersing time by 0,5 - 1 minute for every new sample to be etched in the same solution. The picric acid solution is a color etching technique that allows the visualization of the solidification pattern as dendrites or dendrite-like shapes, but in this case, it was used for grain boundaries reveal to clarify the crack propagation paths.

4.2.2. Microscopy and SEM analysis

Optical microscope Zeiss Axio Imager.M2m with the software Axiosvision was used after etching, while SEM Zeiss Sigma VP was used for fractured specimens, magnification of 69X to 200X, to study potential differences between areas of those samples subjected to different R values.

Furthermore, Energy-Dispersive X-ray Spectroscopy (EDS) was used to identify the presence or absence of oxygen on the fracture surfaces, applying it along the crack of a non-broken sample, as well as on the fracture surface. Key specimens for this are those tested at R = 0,1 and R = 0,7.

4.2.3. Roughness measurements

To measure the surface roughness of the fracture surfaces, confocal microscopy was done by using for those samples that were completely fractured under monotonic loads after the fatigue tests.

Since the specimen thickness was 25 mm, the region possible to analyze was about 40% of that, so a volume of about 10 mm length, 3,5 mm width and 250 μm height was scanned. The studied regions were taken between the side and centerline of the cross section, so deviations due crack front curvatures were reduced.

The studied regions are schematically shown in Figure 15, where red rectangle encloses the scanned area, yellow lines enclose the specific analyzed areas and green lines correspond to one dimension profile study. The same is done for fatigue test 1 and 2. There are three analysed regions either for FSR parameters related to areas S_a, as well as for profiles R_a.

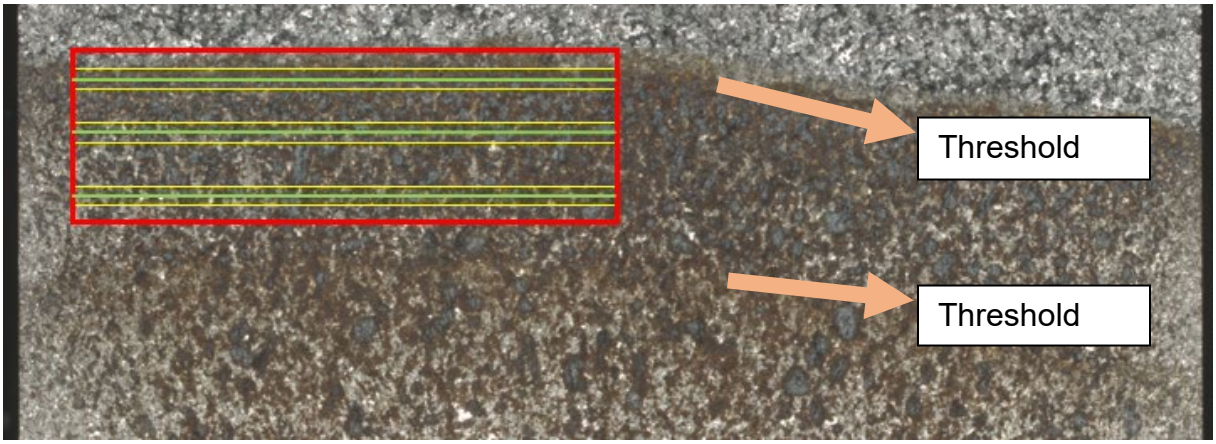

Figure 15 Crack advance upwards, threshold marks and schematic scanned area of the fracture surface region to analyze through confocal microscopy.

Each raw measurement considered a minimum requirement of at least 75% measured points, which were filled out by following the trend of the closest neighboring measured points. Besides, a leveling method was used in case the sample was tilted and the crack advance was deviated through the cross section.

4.3. Application of Kitagawa-Takahashi diagram: Evaluation of ΔK_{th}

Once all ΔK_{th} were obtained, an average was calculated for each series and R value. The diagram is based on two main lines: the first one is given by the fatigue limit $\Delta\sigma_e$, which encloses the top of the security zone, while the second one is a function of $\Delta\sigma$ based on ΔK_{th} through the formula shown previously in Figure 2.

Shape factor “y” was assumed as the same for a penny shaped crack equal to $2/\pi$ [11], because it has the most similar geometry compared to spherical defects given by internal porosities in DCI. It means that Kitagawa-Takahashi diagrams plotted in this study are just an approach to make comparisons easier.

5. RESULTS

5.1. FCG curves and parameters: ΔK_{th}, $\Delta K_{th,eff}$ and K_{max} values for different R

The influence of the R-value, i.e., the quotient between minimum stress and maximum stress for the fatigue testing, on the fatigue crack growth threshold, ΔK_{th}, is shown in Figure 16. Higher R-values result in lower ΔK_{th}, independent of the alloy. In addition, for a fixed R value, the 700 series DCI shows lower values of ΔK_{th}, about 0,5-1 MPa$\sqrt{m}$ below the other grades.

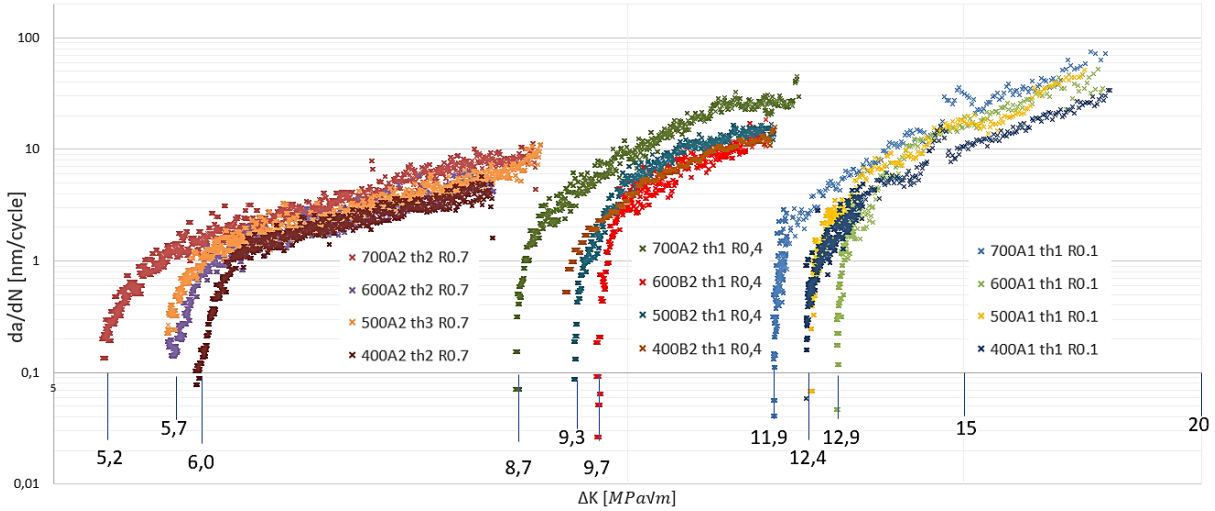

Figure 16 ΔK_{th} for all tested materials at variable R

Despite only the K-decreasing method was applied, it is possible to suggest a stable crack growth following Paris' law for each data set. The vertical part of the curve corresponds to the low-speed propagation whose characteristic value correspond to the threshold. There were peaks due to unstable crack propagations when doing tests like 400A1 and 700A1, but they soon stabilized and is considered not to affect the results significantly.

Table 5 shows the Paris' law parameters for the alloys presented in Figure 17, while Table 8 of APPENDIX D summarizes the Paris' Law parameters for all the samples. The most obvious differences lie on the slopes when testing R = 0,7 and R = 0,1, since m at the highest R tends to decrease around 20% for 600 series, up to 40% lower for other specimens. C parameter is the intercept of the Paris Law line, which was obtained through

a linear regression done over a power law curve, whose variation by orders of magnitude is a consequence of the differences in slope.

Table 5 Paris Law parameters, C in [mm/(lc×ΔK)]; lc = load cycle

Sample	*R*	*m*	*σ (m)*	*C*	*σ (C)*
700A1 th1	0,1	8,26	0,34	3,9E-15	5,9E-15
700A2 th1	0,4	6,91	0,21	1,1E-12	7,2E-13
700A2 th2	0,7	4,68	0,06	3,6E-10	4,8E-11
600A1 th1	0,1	6,04	0,38	1,3E-12	2,4E-12
600B2 th1	0,4	6,27	0,65	2,5E-12	9,5E-12
600A2 th2	0,7	4,81	0,07	1,9E-10	2,9E-11
500A1 th1	0,1	7,44	0,39	2,7E-14	5,1E-14
500B2 th1	0,4	4,87	0,26	9,3E-11	8,2E-11
500A2 th3	0,7	4,44	0,07	4,4E-10	6,7E-11
400A1 th1	0,1	6,26	0,28	4,5E-13	5,2E-13
400A2 th1	0,4	3,86	0,33	8,9E-10	1,1E-09
400A2 th2	0,7	3,88	0,08	1,1E-09	1,9E-10

The effective difference in stress intensity factor, $\Delta K_{th,eff}$ for R = 0,1 behaves like standard ΔK regarding variation of its magnitude, where $\Delta K_{th,eff}$ is between 1-3 MPa$\sqrt{m}$ lower than ΔK_{th}, while at the highest R this difference is maximum 0,2 MPa$\sqrt{m}$.

Despite the case of $\Delta K_{th,eff}$for R = 0,4 follows a similar pattern as described before, it has very spread data as shown in Figure 17 due to variations on force when the crack is opening, i.e., ΔK tends to go up and down at a same da/dN.

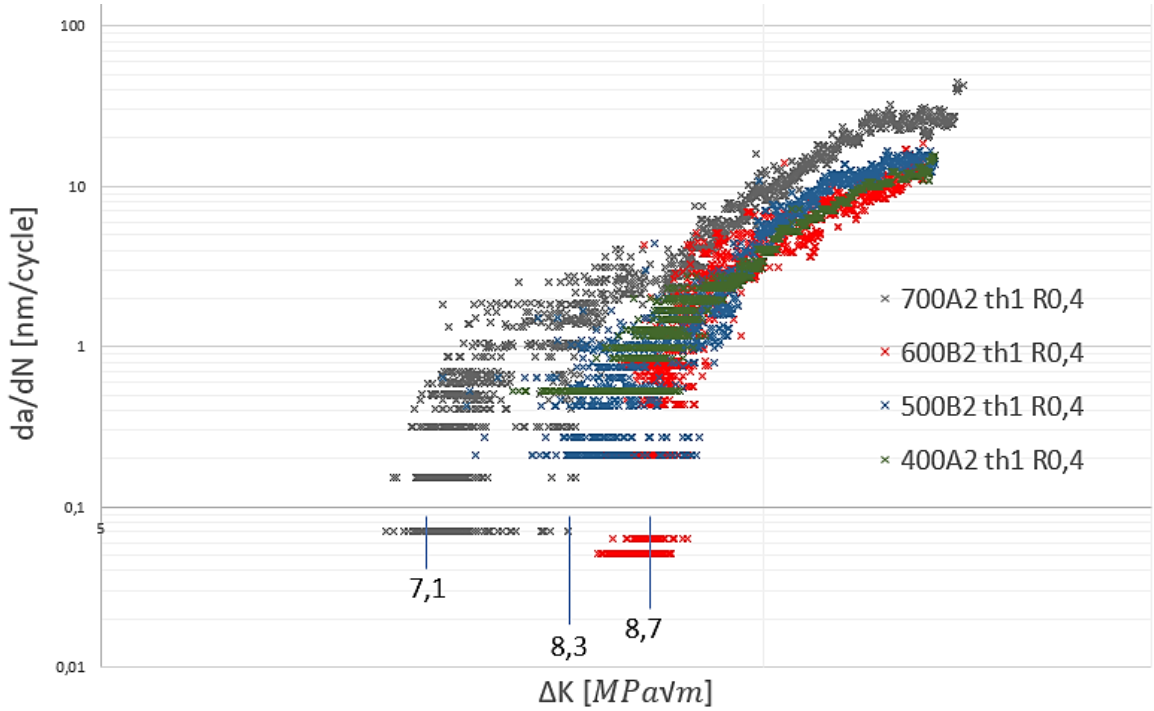

Figure 17 $\Delta K_{th,eff}$ at R = 0,4

Table 6 summarizes all the ΔK values at the threshold. The expression a/W represents the crack advance over the total width, it is significantly higher at R = 0,7 for all the tests since they required a longer initial crack length, moreover it took more cycles to reach the threshold. ΔK max shows a tendence to increase as R also does.

Table 6 Most relevant ΔK values at the threshold, ΔK in MPa√m, σ represents one standard deviation

Sample	R	ΔKth	σ (ΔK_{th})	$\Delta K_{th,eff}$	σ ($\Delta K_{th,eff}$)	$K_{max,th}$	σ ($K_{max,th}$)	a/W
700A1 th1	0,1	11,94	0,01	8,94	0,05	13,27	0,02	0,41
700A2 th1	0,4	8,72	0,02	7,07	0,17	14,55	0,03	0,40
700A2 th2	0,7	5,21	0,03	4,99	0,07	17,33	0,10	0,59
600A1 th1	0,1	12,88	0,02	9,66	0,02	14,31	0,03	0,39
600B2 th1	0,4	9,67	0,02	8,74	0,22	16,13	0,03	0,36
600A2 th2	0,7	5,70	0,02	5,66	0,03	19,00	0,08	0,54
500A1 th1	0,1	12,46	0,05	11,36	0,06	13,84	0,05	0,39
500B2 th1	0,4	9,34	0,04	8,33	0,31	15,57	0,06	0,37

500A2 th3	0,7	5,60	0,03	5,46	0,04	18,69	0,10	0,59
400A1 th1	0,1	12,34	0,04	10,28	0,07	13,71	0,05	0,40
400A2 th1	0,4	9,11	0,02	8,51	0,23	15,24	0,02	0,37
400A2 th2	0,7	5,96	0,01	5,96	0,01	19,87	0,03	0,53

Moreover, every ΔK_{th}, $\Delta K_{th,eff}$, and $K_{max,th}$ for each tested sample can be seen in Table 7 in APPENDIX D.

5.2. FCG along the microstructure

5.2.1. Fatigue crack growth paths

Cracks propagate through the matrix both intergranular and transgranular, as shows Figure 18. (a) 400C2 shows how the crack tip advanced around a graphite particle, went through a ferrite grain and around the next one, at the next graphite particle, the crack grew around it until encountering a non-ferrite particle where it seems to stop.

Figure 18(b) 400C2 shows a crack near the threshold. In this case the crack grew through the graphite, then it branched, and the secondary crack kept growing mainly transgranularly. Both Figure 18(c) and Figure 18(d) 500B1 revealed cracks with both trans and intergranular propagation due the level of ΔK reached during the test (1-3 MPa$\sqrt{m}$ higher than the threshold value).

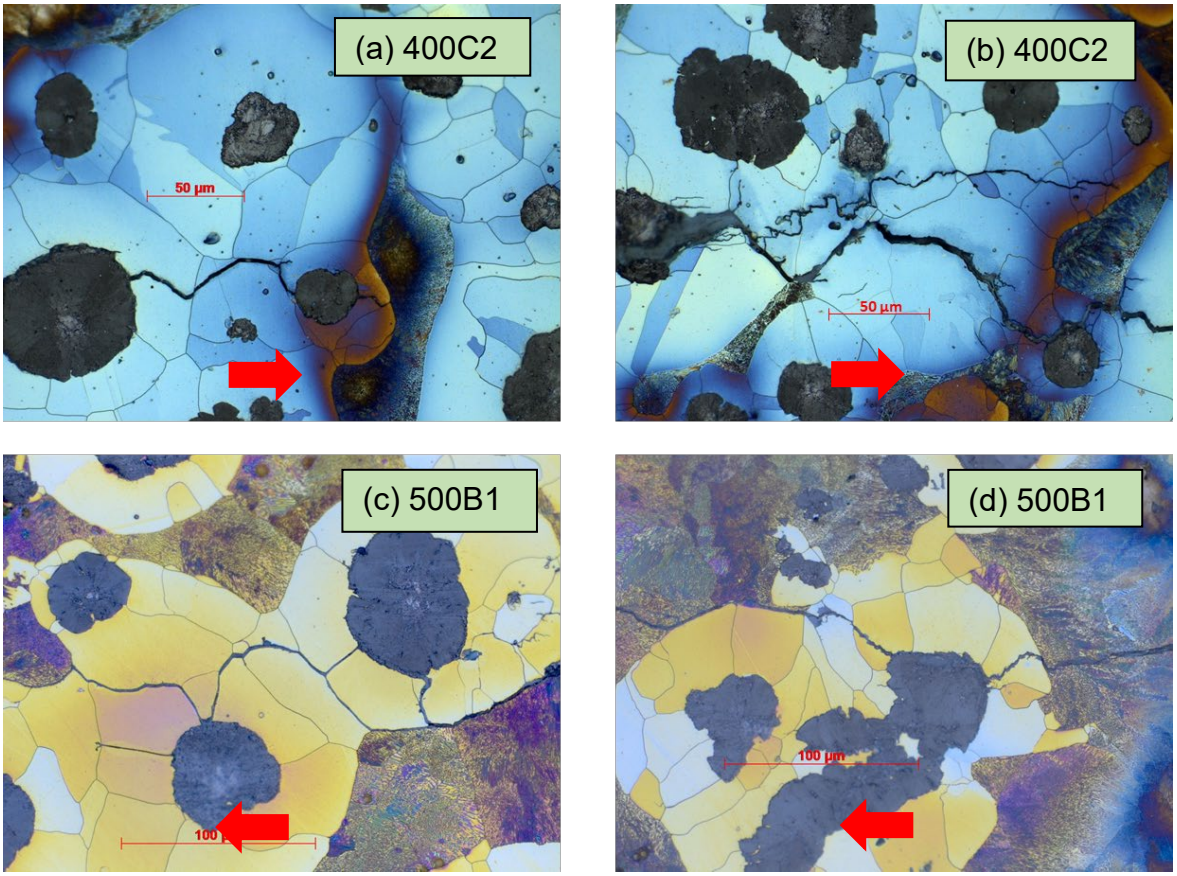

Figure 18 Inter- and transgranular crack propagation over 400C2 and 500B1 specimens at R=0,1 Red arrows indicate crack growth direction. Picral etching, 500X magnification

Figure 19 presents the microstructure of four DCI showing cracks. Higher R values cause a smaller crack width clearly seen comparing Figure 19(a) with Figure 19(d). Figure 19(c) shows the transition from R = 0,4 to 0,7 in the middle, where the crack width is reduced. Despite 600B1 has some vermicular graphite (see Figure 19(b)), the crack still grows mainly around graphite particles until the angle is not favorable enough.

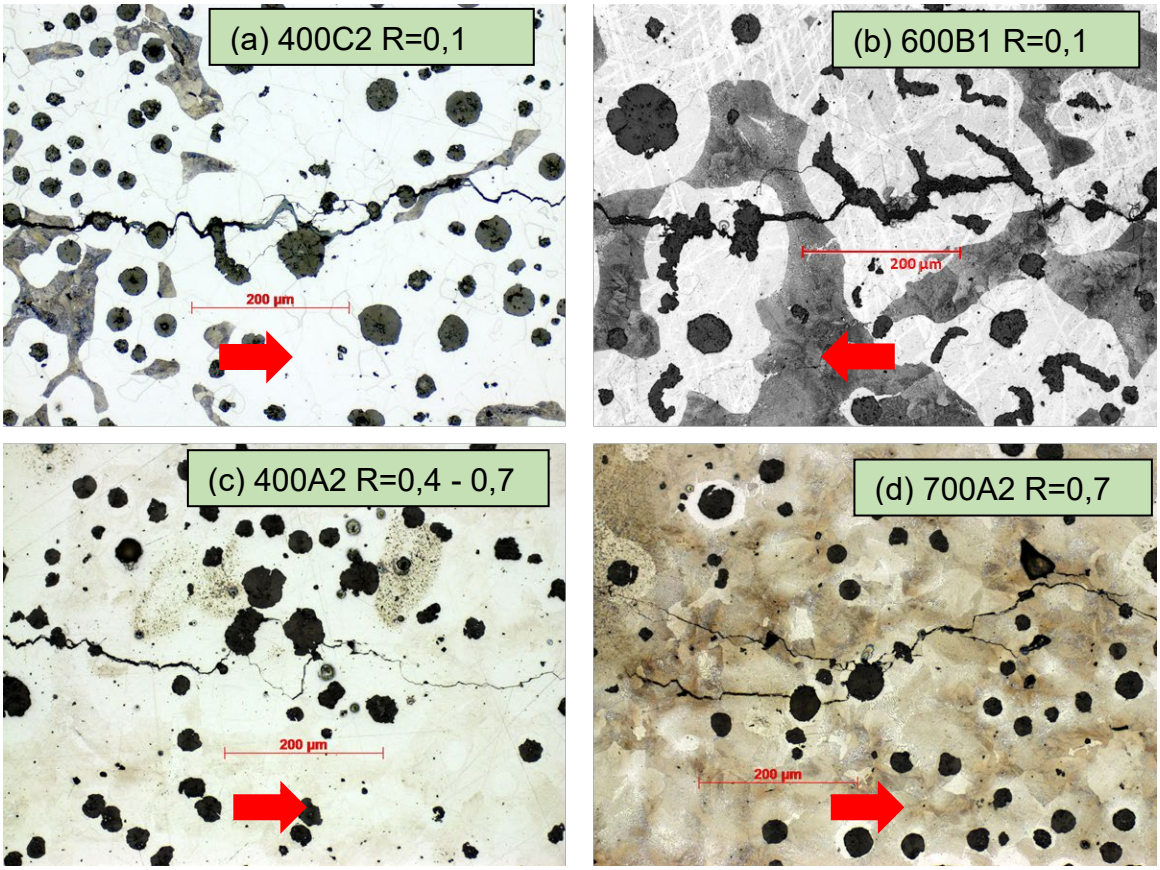

Figure 19 Crack propagation over each DCI series at different R, red arrows indicate their growing direction. Nital etching, 200X magnification

5.2.2. Crack tips and branching

Cracks can branch independent of matrix, R and ΔK as depicted before in Figure 19. Secondary cracks might grow from weak neighboring zones and keep growing until they eventually join the main crack, or just stop growing because the surrounding stresses are not high enough.

Such branching may start from graphite particles as shown in Figure 20(a). The crack grows from the left side at a direction that coincides with the pearlitic lamellae orientation (see Figure 20 (b)), until it encounters a ferritic grain boundary. After that, the crack immediately switches direction and continues its propagation along the graphite boundary. Though it is not possible to know which of next cracks grew first, they encounter next graphite and keep going around to connect with another one. It shall also be emphasized that the analysis is performed on a two-dimensional image while the actual crack growth occurs in a three-dimensional space.

a) b)

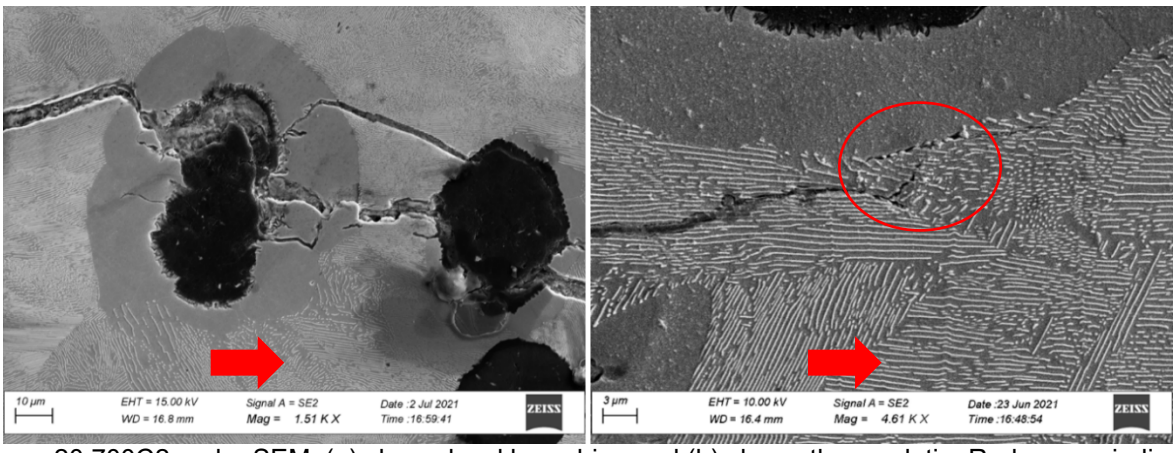

Figure 20 700C2 under SEM: (a) shows local branching and (b) shows the crack tip. Red arrows indicate crack growth direction

It is common to find either some branching or non-connected cracks at the tip. These seem to be ahead of the primary one, no matter the R value nor matrix structure as Figure 21 shows. Figure 20(b) also indicates this similitude for 700C2, where the crack is coming from the left through pearlitic lamellae in a favorable orientation, then it meets another pearlite grain boundary and try to reach the ferritic boundary. Within the marked area in Figure 20(b), a barely visible crack emerges in between the pearlite and ferrite boundaries, which is apparently not connected, at least in the current plane, with the main one.

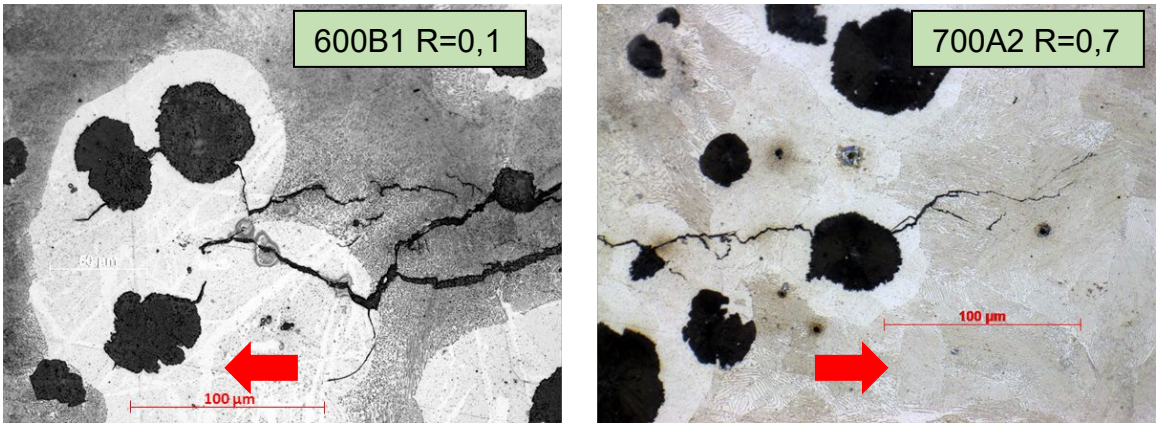

Figure 21 Crack tips on nital etched samples 600B1 at different R. Red arrows indicate crack growth direction. 500X Magnification

5.2.3. Fractured surface overviews of 400 and 700 specimens

For 700 A1 sample, Figure 22(a) shows clear signs of oxidation in region 1. Region 2 encloses a cleavage in pearlite where some river-like paths are seen. Figure 22 (b) shows a cleaner surface due the absence of oxidated areas.

a) b)

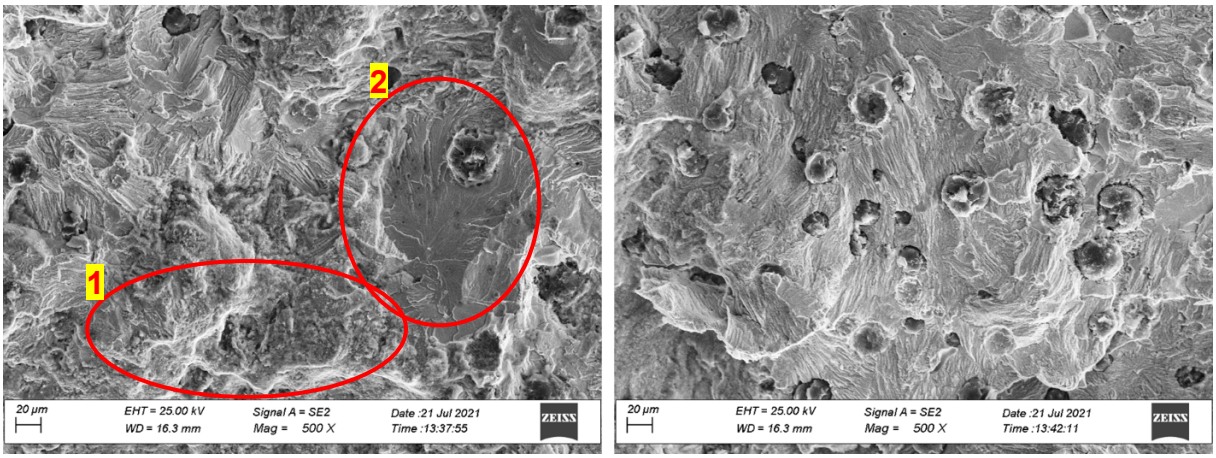

Figure 22 Fractured surface of 700A1 sample at R = 0,1. (a) Region near the threshold and (b) Far from the threshold

While for 400 A1 sample, Figure 23 (a) shows about the same proportion of both, inter and transgranular fracture, where the first is depicted by smooth surfaces, while the second has an appearance mainly rough. This can also be observed in Figure 23 (b) at a higher magnification

Some samples suffered graphite debonding as shown in Figure 23(b), however, graphite nodules in general tends to remain compact, leaving clean round holes. Besides, clear intergranular fracture through ferrite is visible, leaving such geometrical pattern on the surface.

a) b)

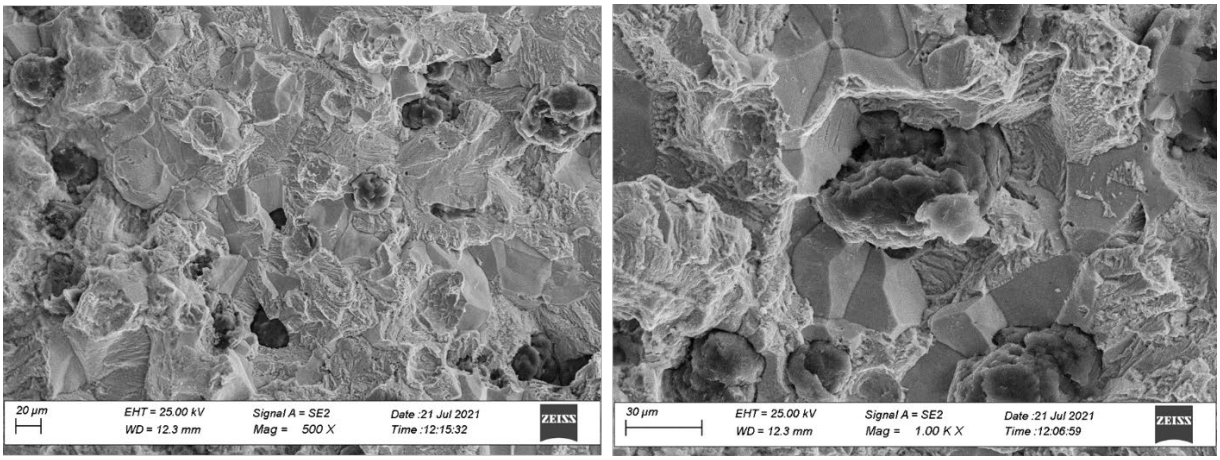

Figure 23 Fractured surface of 400 A1 sample. (a) Overview of inter-transgranular fracture (b) Signs of intergranular fracture around the central graphite

Differences between fracture mechanisms in 700 and 700 specimens, i.e., pearlitic and ferritic matrix are related to their appearance, since in Figure 22 it is not easy to state which grains had inter or transgranular fracture because of the river-like paths and the lamellar structure proper of pearlite.

5.3. Crack closure impact on FCG

5.3.1. Opening force at different R

Figure 24(a) presents the forces applied to the 700 series DCI as a function of cycles at R=0,1. If there were no crack closure phenomenon, the maximum force would correspond to the sum of ”force opening” and the “force peak-peak”, as it happened in Figure 25(c) for R=0,7. However, it is shown in Figure 24(a) that after $5x10^5$ cycles the sum of both forces (orange and blue data) are higher than the force max. Such difference corresponds to the true opening force, i.e., the force required for the crack to open.

Figure 24(b) has more spread data in force opening due to the instability of the crack closure, i.e., there is a mixed behavior at R = 0,4 where the sum of the forces (blue and orange data) varies between being equal or higher than force max.

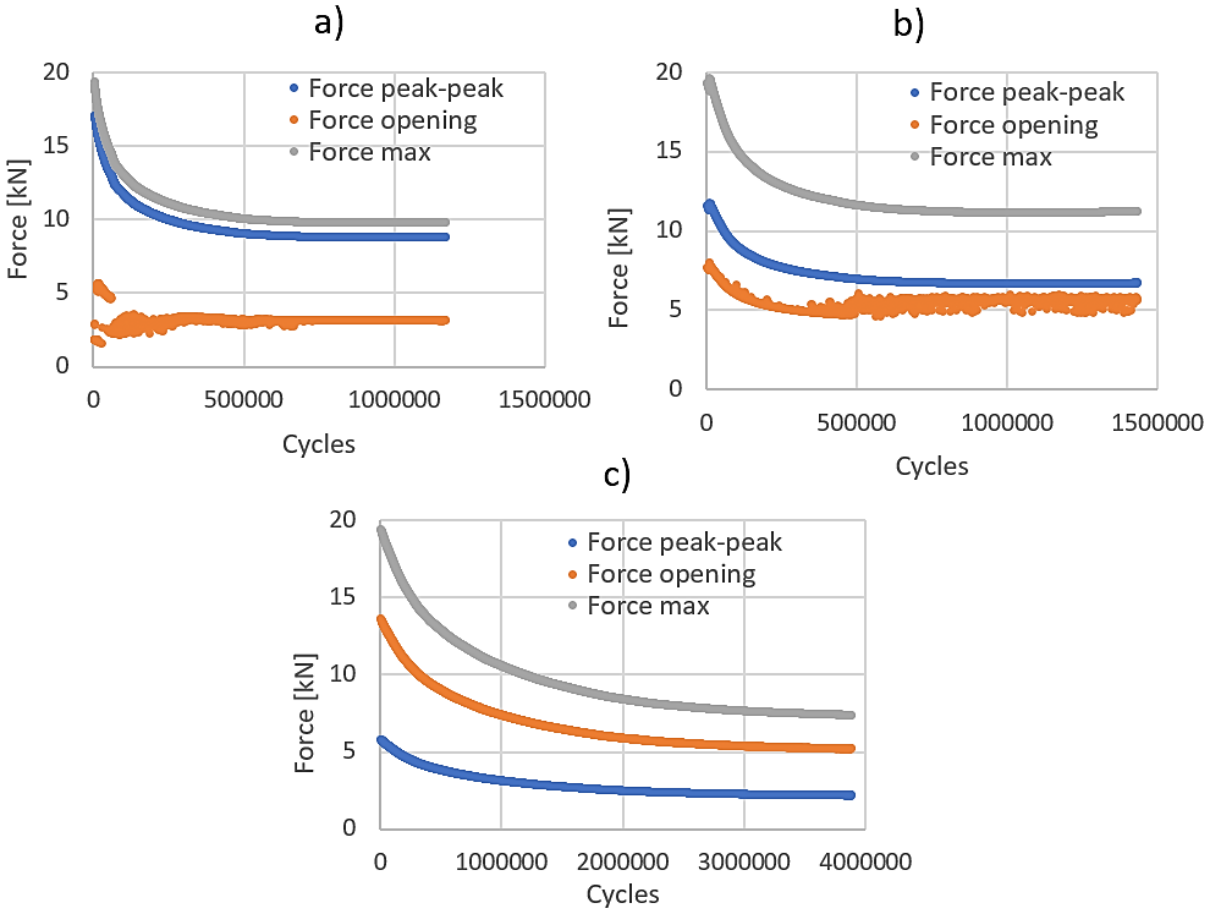

Figure 24: Force applied to different DCI: a) 700 A1 at R=0,1; b) 700 A2 at R=0,4 and c) 700 A2 at R=0,7

Figure 25 presents ΔK as a function of cycles that behave in consequence with the force relations from Figure 24. It is observed that, first, the ΔK tends to the ΔK_{eff} for high values of R. Second, the ΔK value is higher for a lower R value and third, the same scatter is seen at R=0,4 after $5x10^5$, as illustrated in both Figure 24 b) and Figure 25 a).

Differences between standard ΔK and the effective one are not observed in for R = 0,7 until $2,5x10^6$ cycles, where ΔK effective tends to go slightly below standard ΔK at the threshold. Moreover, all samples tested at high R reached the threshold after 3 million cycles, while for those subjected to R = 0,4 and 0,1 this is achieved around 1 million cycles.

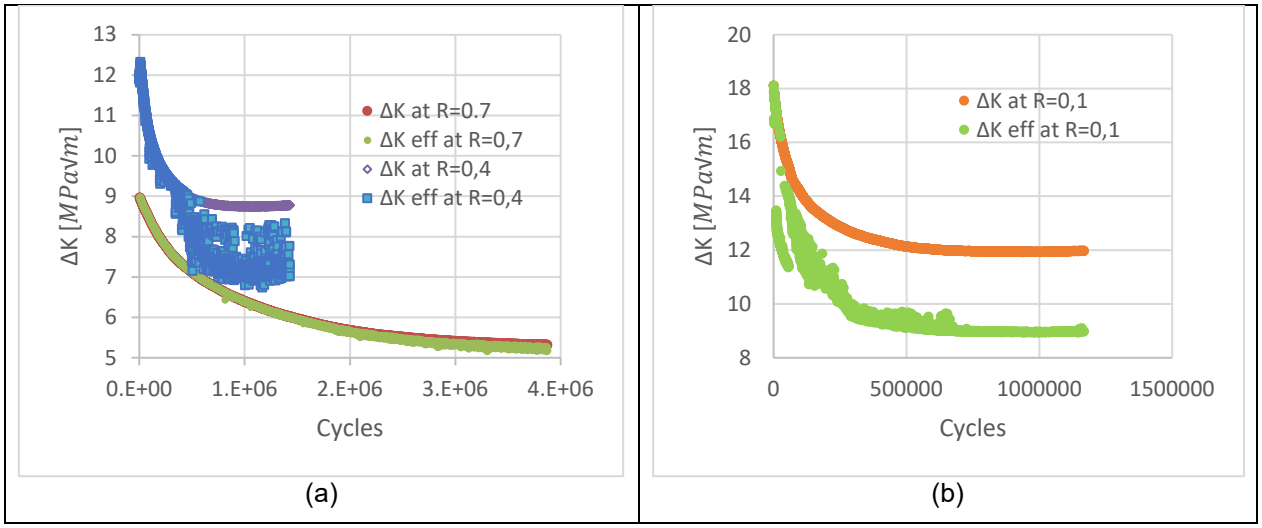

Figure 25 ΔK standard and ΔK effective along the cycles for: a) 700A2 at R = 0,4 and 0,7; b) 700A1 at R = 0,1.

5.3.2. Anomalous crack length measurements

Crack mouth elongation Δv and force peak-peak ΔP as function of the number of cycles are shown in Figure 26(a) and Figure 26 (b), respectively, for 400 A1 after high cycle test. ΔP and Δv for region 1 at 1 million cycles correspond to 7,8 kN and 0,075 mm respectively, while for region 2 at 3 million cycles correspond to 8,1 kN and 0,080 mm. It means ΔP increased by 3,9% and Δv by 6,3%. Besides, after 2 million cycles the opening force tends to show an increase in data dispersion.

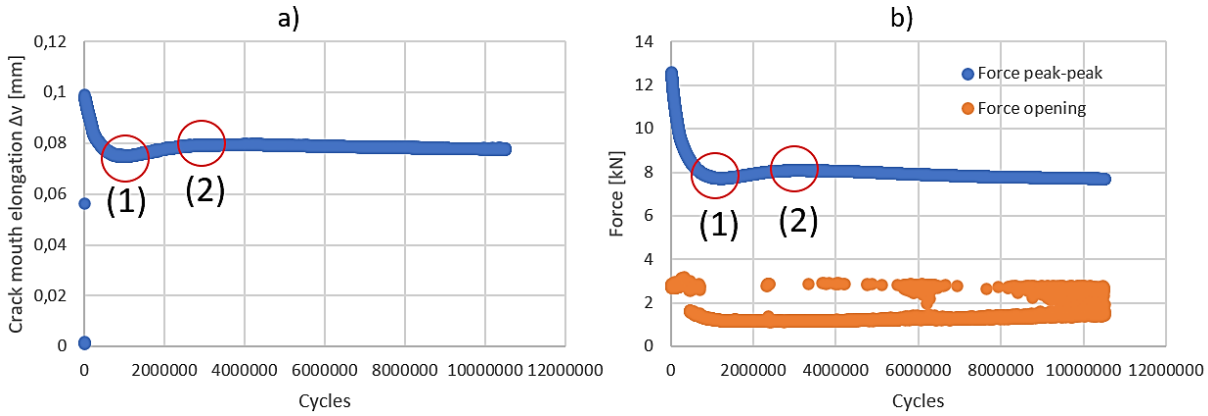

Figure 26 a) Crack mouth elongation and b) Force along the cycles for 400 A1, test #2

When the tests were long enough at R = 0,1, it was common to see an apparent decrease in crack length once ΔK_{th} is reached, i.e., around 1 million cycles. A similar trend, although

less pronounced, can be seen for tests at R = 0,4 but not for tests at R = 0,7, as Figure 27 illustrates.

Figure 27 shows that for the sample 400A1 the crack length reaches a maximum value of 24,5 (mm) at around $1X10^6$ cycles, from which an apparent decrease can be observed up to ~$2X10^6$ cycles, then it remains relatively steady from cycle $2X10^6$ and up. The aforementioned represents the impact of variations in ΔP and Δv shown in Figure 27. Something similar is observed for the sample 400B2 in which the maximum crack length is approximately 23 mm. On the other hand, the sample 600A2 reaches a maximum crack length of around 27 mm.

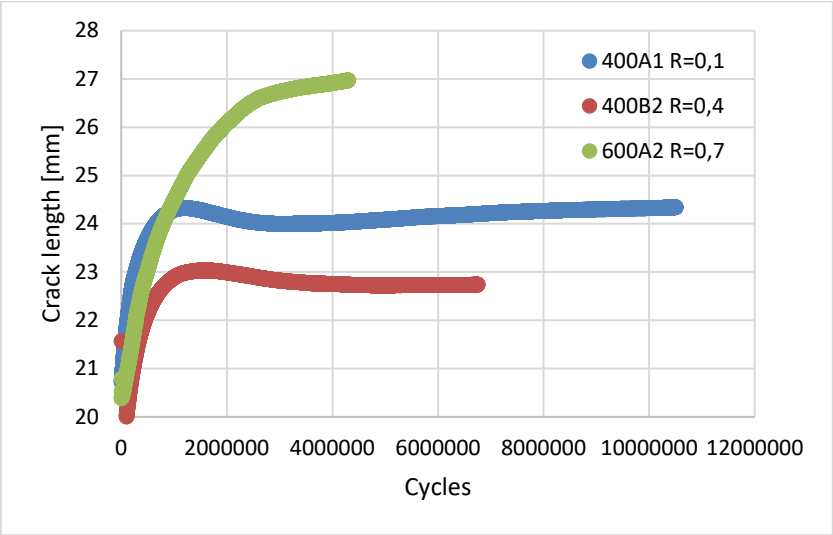

Figure 27 Crack length as a function of load cycles during high cycle tests.

5.3.3. Fracture Surface Analysis

Figure 28 shows fractured surfaces for different samples tested at R=0,1, 0,4 and 0,7. Oxidation is observed in the three samples presented as a dark contrast in the lower part of each micrograph (red circle). The main difference is depicted in sample 600 A2, where first test under R = 0,1 have marked oxidation layers on the fracture surface while the second ones do not. For R = 0,1 and 0,4 there is a clear border between test 1 and 2, i.e., a clear difference in appearance with a darker line at the end of each test. The change in appearance seem to start earlier for R=0,1, is still clear for R=0,4 but not seen for R=0,7.

Looking at the crack front advance, a marked curvature can be seen in all fractured samples at R = 0,1 and 0,4. These curvatures can be symmetrical from the center as in test 1 for 400 B2 and 600 A2, or uneven from the sides as for 400 A1. For the test performed at R=0,7, no curvature can be observed.

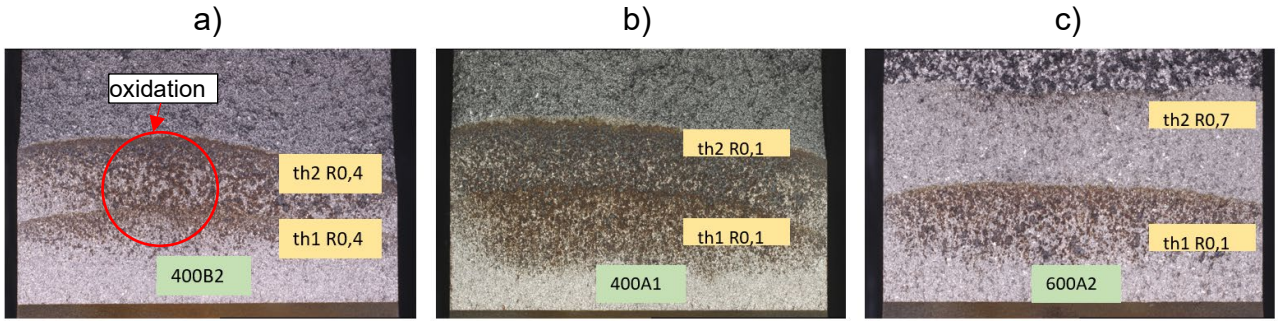

Figure 28 Overview of fracture surfaces at different R values: (a) 400B2 at R=0,4, (a) 400A1 at R=0,1 and (a) 600A2 at R=0,1 – 0,7.

The cross-section image to the left in Figure 29 shows that the crack has been filled with a second phase (different contrast as the matrix that surrounds that graphite particles). EDS analysis near the crack tip on the center line of sample 400C2 tested at R=0,1 show a clear presence of oxygen as shown by the turquoise region to the right in Figure 29. Another EDS done on the crack of the same specimen, but far from the tip, shows similar levels of oxygen, even present in a neighbor branching.

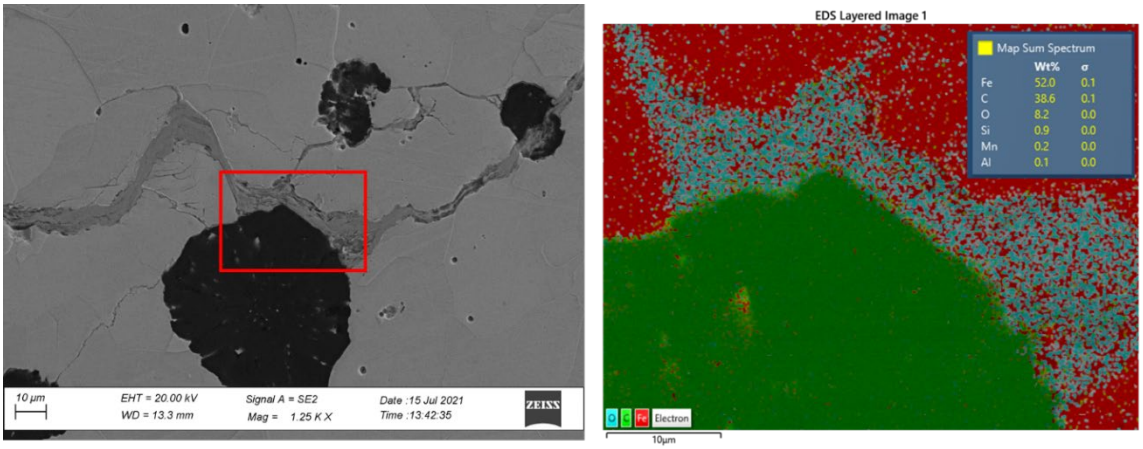

Figure 29 18 SEM and EDS analysis near the crack tip for 400C2 sample tested at R = 0,1

The fractured surface of 600A2 is shown in Figure 30. At the end of test 1 at R=0,1, around 10% oxygen is present, while at the beginning of test 2 no oxygen is detected. The EDS analysis at the end of test 2, shows 2% oxygen was present, randomly distributed.

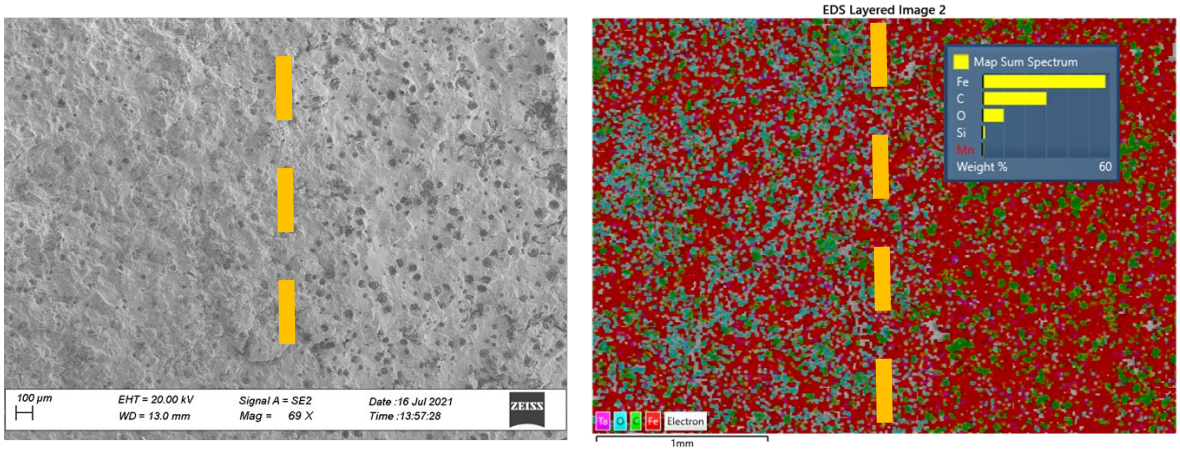

Figure 30 SEM and EDS analysis of 600A2 fractured of test #1 at R = 0,1 to the left of the dashed line and test #2 at R = 0,7 to its right for both images

5.3.4. Fracture surface roughness

Figure 31 a) shows the surface roughness, Ra, for the different DCI tested a R=0,1. The 600A1 DCI shows the highest Ra (12 to 16 µm), while for the other materials Ra varied in the range 8-13 µm. Most of the analyzed samples tend to have a tendence to decrease as ΔK decreases. Figure 31 b) indicates the same behavior, no matter the R at which the samples are subjected to. There is no clear influence of R-values over Ra, since 600A2 has lower Ra at high R, the opposite occurs for 400A1 and 400B2 samples, while for 500A2 it looks more even.

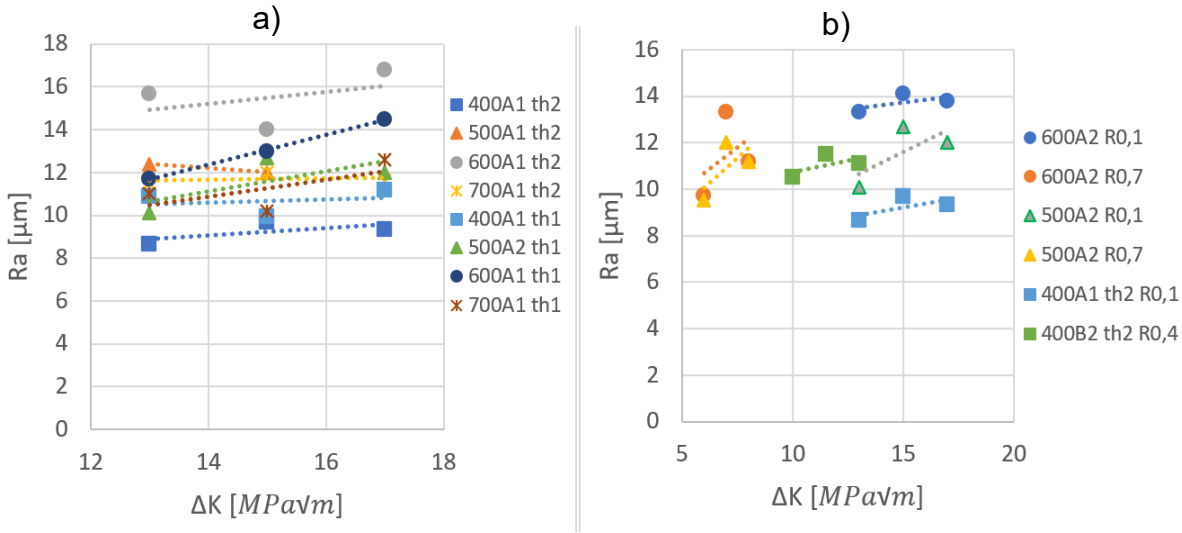

Figure 31 (a): Ra for different materials at R = 0,1; (b): Ra for two different R per material

Analogously, Figure 32 a) shows Sa values that tend to increase along with ΔK. The lowest Sa is about 20 µm and belongs to 400A1 sample, the highest is between 40 and 50 µm for the other materials, but as an average these values move between 30 and 40 µm. As for Ra, Figure 32 b) evidences no influence of R over Sa and more data would be needed to establish a relationship.

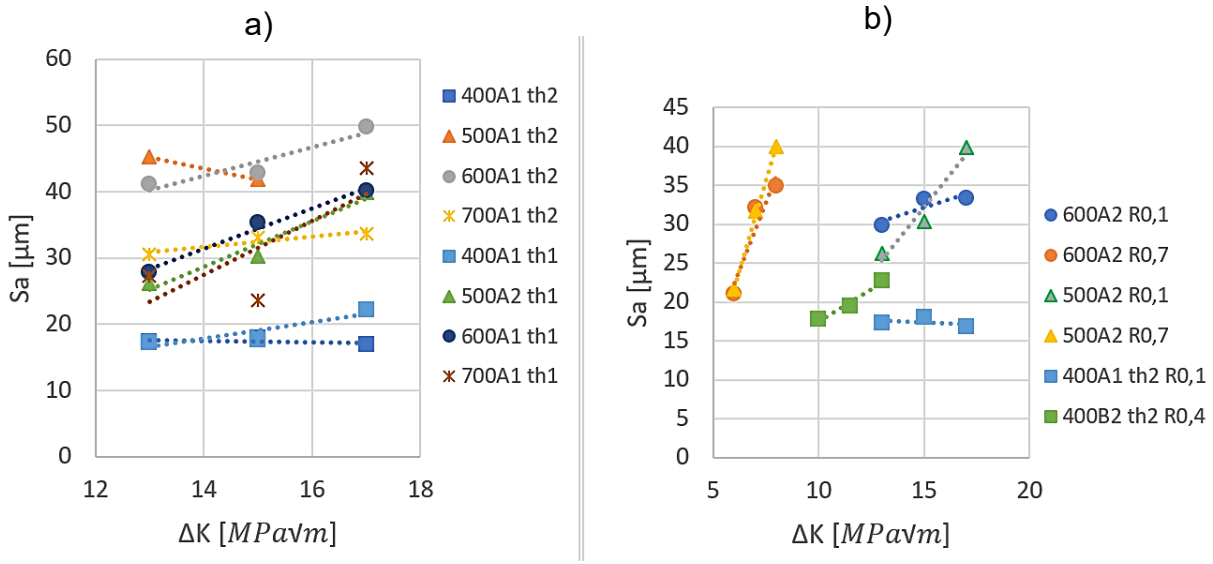

Figure 32 (a): Sa for different materials at R = 0,1; (b): Sa for two different R per material

5.4. Kitagawa-Takahashi diagram

Four top limits were plotted, i.e., one line based on the regarding $\Delta\sigma_e$ for each DCI series. Due to their similitudes in ΔK_{th} for every R value tested, Figure 33 shows how small are the gaps between the side limits for each series in a zoomed graph with a very narrow scale at R=0,1. To avoid such overlapping of the side limits, only those with the smallest ΔK_{th} were plotted, which correspond to the 700 series for each R as shown in Figure 34.

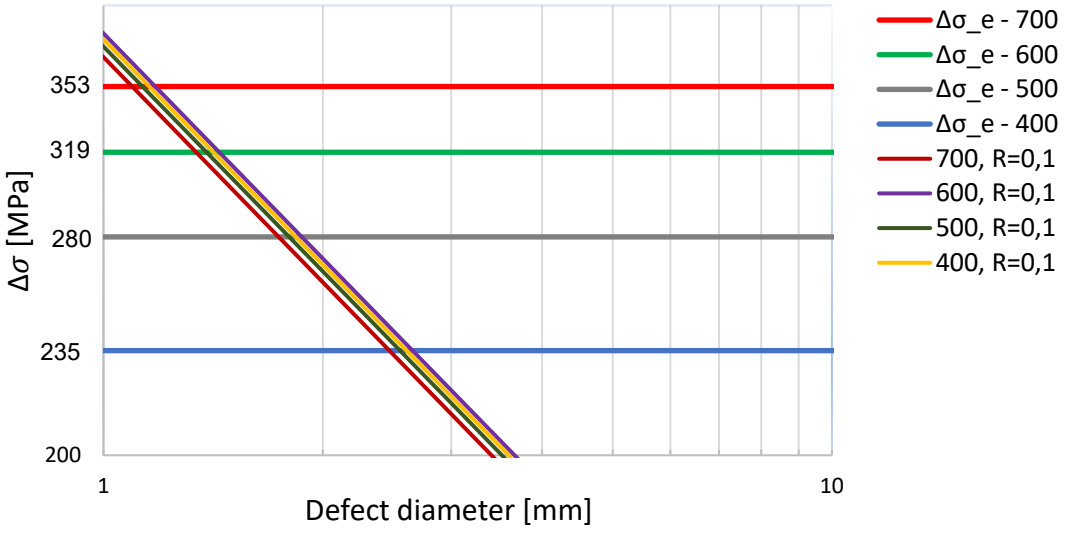

Figure 33 Kitagawa-Takahashi diagram for each DCI series at R=0,1

From Figure 34 it is possible to compare the fatigue resistance for each DCI series based on the external $\Delta\sigma$ applied and their potential defect sizes. For example, if a DCI 400 series is subjected to its fatigue limit (235 MPa), it would stand just at the limit of the security zone for defect sizes smaller than 2,5 and 2 mm diameter for R=0,1 and 0,4, respectively. However, if either the defect is bigger or the $\Delta\sigma$ is higher, an imminent crack would start to propagate. The same would happen for a DCI 700 series if the $\Delta\sigma$ is kept at 235 MPa.

On the other hand, if a DCI 400 series is subjected to $\Delta\sigma$ = 300 MPa, it will fracture no matter how small the defect is nor its R, while a DCI 700 series would tolerate it with defects up to ≈ 1,5 mm diameter for R=0,1. Not so in the case of R = 0,4 nor 0,7, unless the defects were up to ≈ 1 and 0,4 mm respectively.

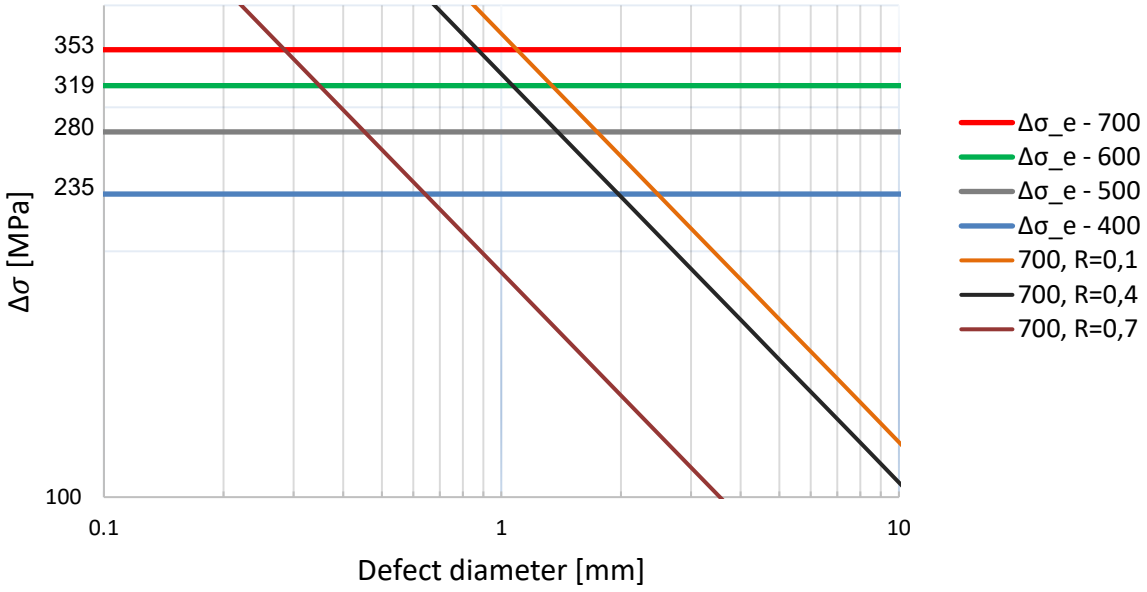

Figure 34 Kitagawa-Takahashi diagram for each R

5. DISCUSSION

First, it should be mentioned that the micro- and macrostructure and, hence, the properties will be different among the various DCI series and as well as within cast iron parts. By establishing this, the results presented in this work may not be representative for all cast iron parts with different geometries. In this study, samples B and C are from Y-blocks of different thicknesses and of the similar orientation within the Y-block. The difference in thickness, 50 respectively 75 mm, did not cause a clear difference in ΔK_{th}. This difference in thickness, or more specific solidification and cooling conditions are however rather small, and more studies are needed to investigate if thickness, or rather microstructural coarseness will influence the crack growth behavior.

The crack length at which the $\Delta K_{th}$is obtained has a considerable impact on the threshold value, hence, the evaluation must be done in the same way for all materials. Table 6 shows that the a/W ratio was around 0,4 for samples ran at R=0,1 and R=0,4. For R=0,7, the FCG rate tended to decrease slower and a/W was around 0,55, which means that ΔK_{th} might be slightly overestimated, since longer cracks tended to show higher threshold values as described in APPENDIX A.

Comparing the values of ΔK_{th} obtained in the present study with results in the literature [19], [29–32], they show the same behavior around the different R-values, i.e., the cracks propagate around the graphite particles, they also tend to branch towards other favorable orientations and the fracture mechanisms are both trans-intergranular. The materials studied here also have similar ΔK_{th}, whose differences lie on about 1 MPa$\sqrt{m}$ higher for series tested at R=0,7 and up to 2 MPa$\sqrt{m}$ at R=0,1.

Regarding the slopes in the Paris region, there is a tendency to decrease if R is increased, which also happens for other authors either for DCI or steels [19], [33], [34]. This might be explained by the high magnitude of ΔK at R=0,1 compared to that with a higher R, so, as ΔK is the driving force behind FCG, it results in faster crack growth rates at such region.

Crack closure influence is clearly seen through $\Delta K_{th,eff}$ for different R, regardless the series. An R value of 0,1 has the most significant variations regarding ΔK_{th} because the

minimum force applied by the machine is lower than the force required to open the crack. In contrast, R=0,7 has almost equivalent ΔK_{th} and $\Delta K_{th,eff}$, since the minimum force is high enough to leave the crack open during the whole load cycle.

The crack has a mixture behavior at R=0,4, i.e., it takes turns between leaving the crack partially opened and closed, because the minimum force tends to get closer to the opening one. Besides, the scattered data at this R can be a consequence of variations in such opening force on each cycle along the crack growth, which can be given mainly by roughness, amount of surface in contact and local plastic deformation near the tip.

$K_{max,th}$ has a tendence to increase along with R-values, unlike to what Heine *et al.* [19] reported for DCI 700 series, showing an overlap of the FCG curves. However, it can be explained by a second threshold $K_{max,th}$ that must be overcome together with ΔK_{th} to let the crack grow as Figure 35 illustrates, since their values are material and R dependent. So, the researchers' tests went through both thresholds at the same or very similar time because their $K_{max,th}$ was fixed for all the R-slopes according to their material features, whereas the 700 series tested at R > 0 for this paper overcame $K_{max,th}$ first and ΔK_{th} after a while, so $K_{max,th}$ kept increasing until both were reached.

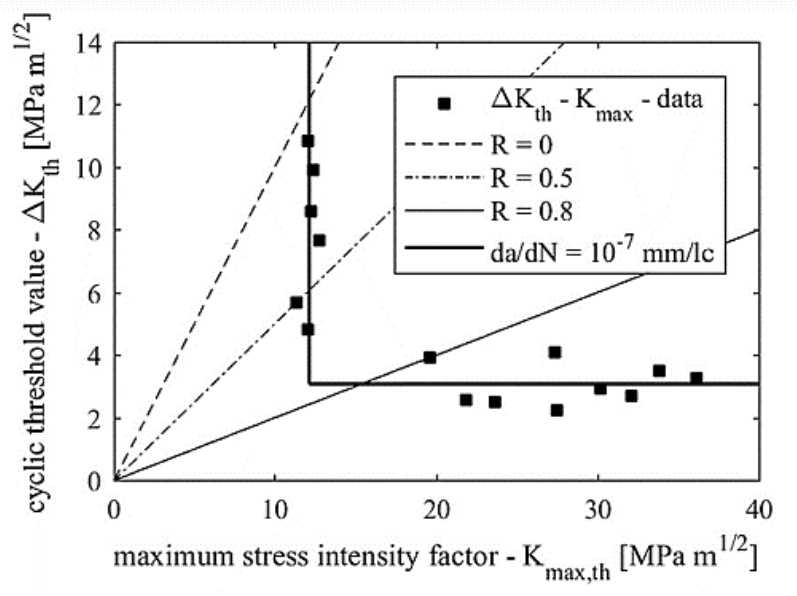

Figure 35 Correlation between $K_{max,th}$ and ΔK_{th} [19].

Cracking patterns are the same for all the specimens regardless of their matrix or their R-values. The crack propagates mostly around the graphite particles no matter their nodularity, while in more isolated cases it goes through them. Its propagation along the matrix is both trans and intergranular, which is clearer seen in ferrite. Besides, the crack tends to prefer the ferrite-perlite interface when approaching the next graphite.

It is common to see crack branching, whose origin might come from an extension of the main crack, or from a close-lateral side. These could branch due to a weak neighboring zone with close surrounding graphite particles, as well as high stress concentration in several directions that can also be mixed with residual stresses. It might be somehow beneficial, since the energy is released in another direction, decreasing the crack growth rate in the main crack.

There are cracks ahead of the crack tip that do not look connected. It could be that such crack ahead was originated from an independent non propagating crack, so it eventually became a crack due to higher stresses produced when the crack tip got closer, similar to what Iacoviello et al. reported [35] . Another point of view would come from a 3-dimensional analysis since the crack ahead might be connected to the crack tip somewhere behind the 2D images.

Iacoviello et al. have described before [32], variations in ΔK_{th} are conditioned by the quality of graphite-matrix interface and graphite shapes for 400 series. Such quality depends on solidification conditions, heat treatments and spheroidizing elements that can modify the interface and graphite properties. They reported the highest ΔK_{th}≈ 13 MPa$\sqrt{m}$ for slow cooling condition with a resultant inhomogeneous microstructure that included chunky graphite, which is about the same for 400 series studied here.

As it was shown for the ferritic DCI tested at SCANIA, the crack growth arrest given by the effect of roughness induced crack closure that Iacoviello and collaborators described can also be achieved through a material with a more homogeneous microstructure, avoiding the detrimental qualities proper of chunky graphite.

Moreover, the main crack growth arrester mechanism near the threshold seems to be the roughness induced crack closure given by the graphite particles. As the crack goes around

them, it must change its direction and so the angle into a less favorable, i.e., it cannot keep its perpendicular tendency to the load. Then, once the crack is ready to go through the matrix again, it encounters a rather round interface that will require a higher stress to be overcome than if the crack tip were flat.

The importance of graphite-matrix interface lies on the strength of their bond, while for graphite particles it is related to their capability to remain compact, because, if the crack goes through the graphite or it does not go around its more external layer, the effect of roughness induced crack closure would not be at its peak.

Another aspect of roughness is fretting corrosion produced by the mismatch between the crack surfaces that is originated by local plastic deformation. The higher the roughness, the greater the mismatch and, therefore, more crack closure effect is present. Such phenomenon generates oxidation layers that are more pronounced at R=0,1 and almost no existent at R=0,7.

As the FCG rate decreases during K-decreasing method, oxidation is more notorious at the end of the crack advance due to the high number of cycles per distance. These oxidation layers act as a wedge in the crack tip that cause variations in Δv and ΔP, i.e., when the crack is closing, this wedge-like pushes away the surfaces beyond the distance that a clean surface would do. Hence, anomalous measurements might come from fretting corrosion, explaining why it does not happen for R=0,7.

An attempt to correlate fracture surface roughness in terms of either R or Sa parameters and ΔK was developed. It can be suggested that the small tendence to have less roughness towards the threshold may be due the close contact between the surfaces for many cycles, which could produce that oxide layers fill the dimples, while the peaks are flattened due to local deformation. However, further investigation must be done to prove this.

But still, reported roughness values can be used as a reference to compare with other materials tested under similar conditions, such as stainless steels, which have less than half Ra of the analyzed DCI [36]. Analogously, when comparing with other DCI, but from

a heavy section like in [31], Ra can go up to double and it does not imply that ΔK_{th} is improved.

Regarding Kitagawa-Takahashi diagram for such DCI series, it shows that the limits given by ΔK_{th} are practically the same for each material. R has a strong influence on the threshold, it decreases the security zone considerably so that it is a requirement to know at which R a piece is going to be subjected to. Furthermore, it is important to state that this diagram was generated based on a penny-like crack shape, therefore, some deviations could occur in practice since the most common defects are porosities with a spherical geometry.

6. CONCLUSIONS

It has been proven that all DCI studied here have similar ΔK_{th}, whose values are around 12, 10 and 6 MPa$\sqrt{m}$ for R = 0,1; 0,4 and 0,7 respectively, but there can be some deviations when comparing with literature. Such differences are given due to variations in manufacture conditions, i.e., cooling rate, heat treatments and alloying elements that determine the material qualities. Because of this, the in-house testing becomes a requirement if the material is to be evaluated for future engineering applications.

Pearlitic or ferritic matrix has little influence on FCG, since graphite nodules are the main responsible for hindering the crack propagation near the threshold. The stronger the matrix-nodule bond, the better fatigue resistance of the material, because the crack tends to advance through the interface around the nodules.

One of the reasons why these materials have significantly higher ΔK_{th} in comparison to most steels is due to the roughness induced crack closure. As DCI are considered heterogeneous materials, graphite nodules cause crack deflections at the tip, in addition that after overcoming such nodule, the next obstacle is a round-like barrier to go through the matrix. Therefore, stresses are less concentrated as if it were a homogeneous material with a rather flat crack tip.

The plasticity together with roughness induced crack closure influence the increasing area of fractured surfaces implies more friction, specially at lower R values, which was verified through EDS analysis and the amount of oxidation produced by fretting corrosion.

According to Kitagawa-Takahashi diagram, if high mechanical and fatigue resistance is required for the design of a truck part, the DCI with better fatigue limit would be more suitable, since ΔK_{th} limit does not change significantly. However, it is important to realize that the allowable defect criteria would remain the same for all these DCI, i.e., the higher the cyclic stresses that the material is going to be subjected to, the smaller are the tolerable defects within the safety zone.

REFERENCES

[1] P. Childs, *Mechanical Design*, 2nd Editio. Elsevier Ltd, 2004.

[2] “IATF Global Oversight.” https://www.iatfglobaloversight.org/.

[3] R. A. Smith, “Fatigue in Transport: Problems , Solutions and Future Threats,” *Proc. Inst. Chem. Eng. Part B Process Saf. Environ. Prot.*, vol. 76, no. No. B3, pp. 217–223, 1998.

[4] “Scania Year-end Report January-December 2020,” 2021.

[5] SS-EN-1563:2018, “Founding – Spheroidal graphite cast irons,” *Swedish Stand. Inst.*, pp. 1–47, 2018.

[6] ASTM A536-84(2019)e1, “Standard Specification for Ductile Iron Castings,” *ASTM Int.*, 2019, [Online]. Available: www.astm.org.

[7] M. Tisza, “Development of Lightweight Steels for Automotive Applications,” in *Engineering Steels and High Entropy-Alloys*, A. Sharma and S. Kumar, Eds. IntechOpen, 2020.

[8] P. Andresen, B. Antolovich, S. D. Antolovich, S. Becker, and C. Q. Bowles, *ASM Metal Handbook Vol. 19 Fatigue and Fracture*. 1996.

[9] A. A. Shanyavskiy, “Mechanisms and modeling of subsurface fatigue cracking in metals,” *Eng. Fract. Mech.*, vol. 110, pp. 350–363, 2013, doi: 10.1016/j.engfracmech.2013.05.013.

[10] G. Antaki and R. Gilada, *Design Basis Loads and Qualification*. 2015.

[11] T. L. Anderson, *Fracture Mechanics, Fundamentals and Applications*. 2005.

[12] ASTM E647−15e1, “Standard Test Method for Measurement of Fatigue Crack Growth Rates,” *ASTM Int.*, pp. 1–50, 2015.

[13] SS-ISO12108:2019, “Metallic materials – Fatigue testing – Fatigue crack growth

method," *Int. Organ. Stand.*, pp. 1–53, 2019.

[14] M. Mlikota, S. Staib, S. Schmauder, and Božić, "Numerical determination of Paris law constants for carbon steel using a two-scale model," *J. Phys. Conf. Ser.*, vol. 843, no. 1, 2017, doi: 10.1088/1742-6596/843/1/012042.

[15] ASTM-E399-20a, "Standard Test Method for Linear-Elastic Plane-Strain Fracture Toughness KIc of Metallic Materials," *ASTM Int.*, 2020.

[16] A. Arcari, N. Iyyer, M. Kittur, and N. Phan, "Investigations of subcritical crack propagation under high cycle fatigue," *13th Int. Conf. Fract. 2013, ICF 2013*, vol. 6, pp. 5133–5143, 2013.

[17] K. Sadananda and S. Sarkar, "Modified Kitagawa diagram and transition from crack nucleation to crack propagation," *Metall. Mater. Trans. A Phys. Metall. Mater. Sci.*, vol. 44, no. 3, pp. 1175–1189, 2013, doi: 10.1007/s11661-012-1416-x.

[18] W. Elber, "Fatigue Crack Closure Under Cyclic Tension," *Eng. Fract. Mech.*, vol. 2, no. 1, pp. 37–44, 1970, doi: 10.1016/0013-7944(70)90028-7.

[19] L. M. Heine, A. Bezold, and C. Broeckmann, "Long crack growth and crack closure in high strength nodular cast iron," *Eng. Fract. Mech.*, vol. 192, no. September 2017, pp. 24–53, 2018, doi: 10.1016/j.engfracmech.2018.02.003.

[20] R. Pippan and A. Hohenwarter, "Fatigue crack closure: a review of the physical phenomena," *Fatigue Fract. Eng. Mater. Struct.*, vol. 40, no. 4, pp. 471–495, 2017, doi: 10.1111/ffe.12578.

[21] K. Walker, C. H. Wang, and J. C. Newman, "Fatigue crack closure due to surface roughness and plastic deformation," *Adv. Mater. Res.*, vol. 891–892, no. March, pp. 319–324, 2014, doi: 10.4028/www.scientific.net/AMR.891-892.319.

[22] M. Benedetti, J. Heidemann, J. O. Peters, and G. Lütjering, "Influence of sharp microstructural gradients on the fatigue crack growth resistance of α + β and near-α titanium alloys," *Fatigue Fract. Eng. Mater. Struct.*, vol. 28, no. 10, pp. 909–922,

2005, doi: 10.1111/j.1460-2695.2005.00932.x.

[23] R. O. Ritchie, “Mechanism of Fatigue-Crack Propagation in Ductile and Brittle Materials,” *Int. J. Fract.*, vol. 100, pp. 55–83, 1998.

[24] M. H. Mosa, “Crack Tip Behaviuor Under Different Load Ratio,” *Al-Qadisiya J. Eng. Sci.*, vol. 8, no. 1, pp. 14–20, 2015.

[25] D. Kujawski and F. Ellyin, “A Fatigue Crack Growth Model With Load Ratio Effects,” *Eng. Fract. Mech.*, vol. 2, no. 4, pp. 367–378, 1987.

[26] ISO-945-1:2019, “Microstructure of cast irons — Part 1: Graphite classification by visual analysis,” *Int. Organ. Stand.*, 2019.

[27] H. Fredriksson and U. Akerlind, *Materials Processing during Casting*. John Wiley & Sons Ltd, 2006.

[28] S. De Tender, N. Micone, and W. De Waele, “Online fatigue crack growth monitoring with clip gauge and direct current potential drop,” *Int. J. Sustain. Constr. Des.*, vol. 7, no. 1, p. 6, 2016, doi: 10.21825/scad.v7i1.3640.

[29] M. Benedetti, E. Torresani, V. Fontanari, and D. Lusuardi, “Fatigue and fracture resistance of Heavy-Section ferritic ductile cast Iron,” *Metals (Basel).*, vol. 7, no. 3, 2017, doi: 10.3390/met7030088.

[30] M. Cavallini, O. Di Bartolomeo, and F. Iacoviello, “Fatigue crack propagation damaging micromechanisms in ductile cast irons,” *Eng. Fract. Mech.*, vol. 75, no. 3–4, pp. 694–704, 2008, doi: 10.1016/j.engfracmech.2007.02.002.

[31] K. Wakamatsu, N. Shiraki, and R. Fujimoto, “Influence of Chunky Graphite on Fatigue Crack Propagation Characteristics in Heavy Section Spheroidal Graphite Cast Iron,” *Japan Foundry Eng. Soc.*, vol. 1, no. 2019, pp. 1–6, 2021.

[32] F. Iacoviello and V. Di Cocco, “Influence of the graphite elements morphology on the fatigue crack propagation mechanisms in a ferritic ductile cast iron,” *Eng. Fract. Mech.*, vol. 167, pp. 248–258, 2016, doi: 10.1016/j.engfracmech.2016.03.041.

[33] M. Benedetti, V. Fontanari, and D. Lusuardi, “Effect of graphite morphology on the fatigue and fracture resistance of ferritic ductile cast iron,” *Eng. Fract. Mech.*, vol. 206, no. October 2018, pp. 427–441, 2019, doi: 10.1016/j.engfracmech.2018.12.019.

[34] S. Bandgar, C. Gupta, G. Rao, P. Malik, R. N. Singh, and K. Sridhar, “Fatigue crack growth rate behaviour of HSLA steel at varying load amplitudes,” *Procedia Struct. Integr.*, vol. 14, no. 2018, pp. 330–336, 2019, doi: 10.1016/j.prostr.2019.05.041.

[35] F. Iacoviello, V. Di Cocco, A. Rossi, and M. Cavallini, “Fatigue crack tip damaging micromechanisms in pearlitic ductile cast irons,” in *Fatigue and Fracture of Engineering Materials and Structures*, 2015, vol. 38, no. 2, doi: 10.1111/ffe.12215.

[36] T. C. Chen, S. T. Chen, L. W. Tsay, and R. K. Shiue, “Correlation between Fatigue Crack Growth behavior and fracture surface roughness on cold-rolled austenitic stainless steels in gaseous hydrogen,” *Metals (Basel).*, vol. 8, no. 4, 2018, doi: 10.3390/met8040221.

APPENDIX A

When performing the experiments, some small and repetitive differences were found within the same samples between their threshold at test #1 and test #2. Figure 36 shows a clear increase in ΔK_{th} at every threshold evaluation #2 compared to test #1. In most cases this variation was about 0,3-0,7 MPa$\sqrt{m}$, and an isolated case occurred for 400 C2 where ΔK_{th} increased 1 MPa$\sqrt{m}$.

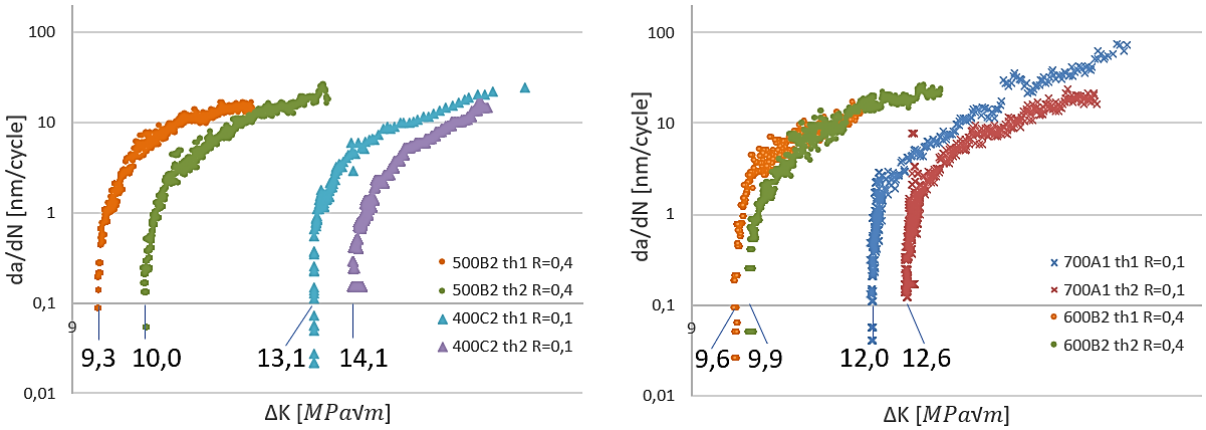

Figure 36 ΔK_{th} at test #1 and test #2 for different DCI and R-value

An estimation of the real crack length was done for all A1 series under microscope for test 1 and 2, which resulted in errors lower than 5% regarding the crack length used by the machine for each test, but the pattern for differences between ΔK_{th} for both tests was still present. Therefore, those variations in threshold were not related to measurements issues.

In order to be consistent, only the results given by tests #1 were considered in the analysis from the tests performed at R=0,1 and 0,4. It does not mean that test #2 results are not valid, but still further studies should be done to explain such differences.

On the other hand, all the tests at R=0,7 were run as a second or third test to have sufficient crack length to collect the data from a high enough da/dN. Because of this, such ΔK_{th} values might be overestimated as it happened in Figure 36.

APPENDIX B

To have a better understanding of the material microstructures, the following section shows the micrographs of each DCI for samples type A, B and C. Figure 37,Figure 38 and Figure 39 were taken at 50X magnification without etching, so that an overview of the graphite particles can be seen clearly. Whereas Figure 40, Figure 41 and Figure 42 were taken at 100X with nital etching to reveal the ferrite and pearlite in the matrix.

Looking at the non-etched pictures, there are no significant differences other than in the case of 600 samples, where several vermicular graphite particles are observed. While for those etched micrographs it is obvious to see an increasing in the pearlite content, which goes from almost fully ferritic matrix in 400 series, to almost fully pearlitic in 700 ones.

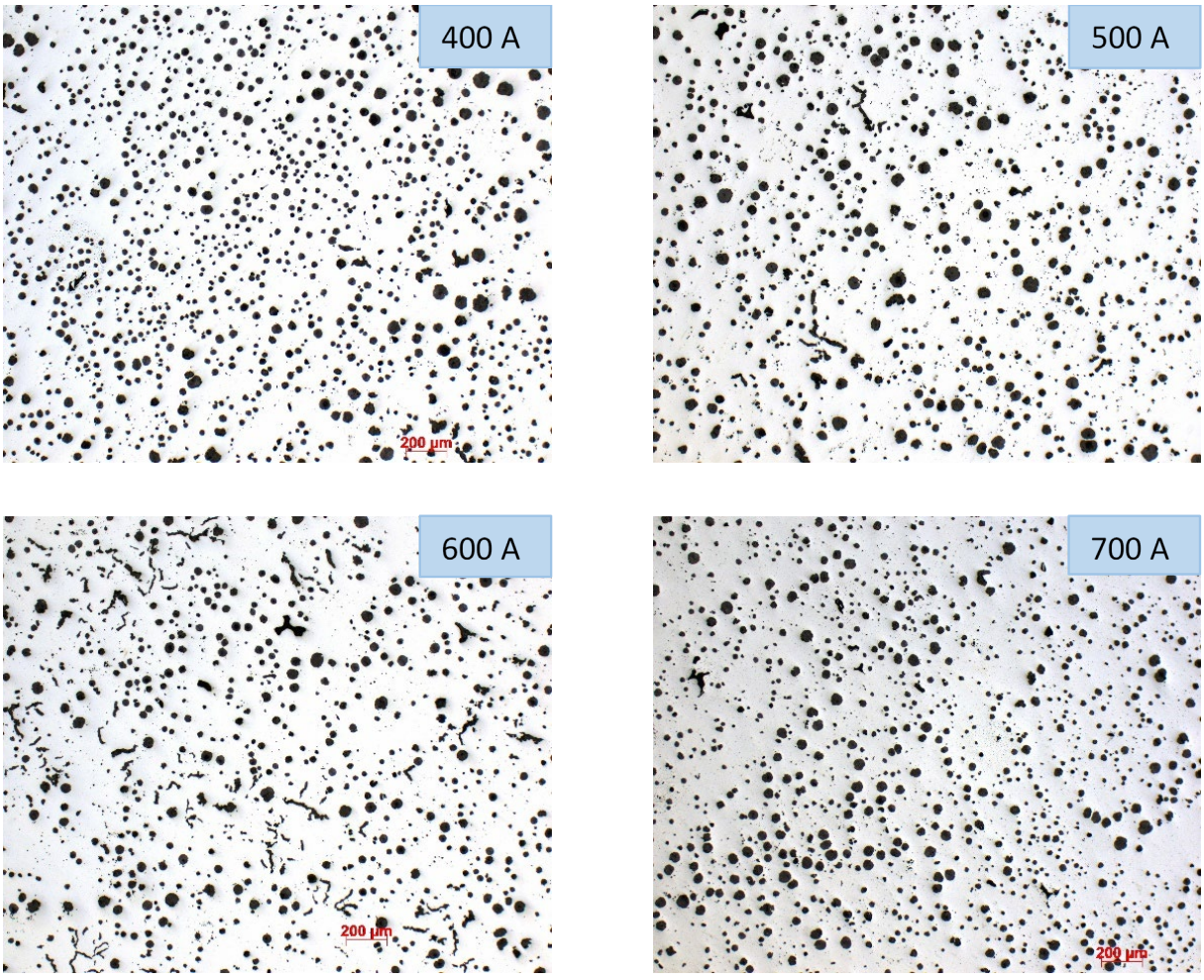

Figure 37 DCI series type A, non-etched. 50X

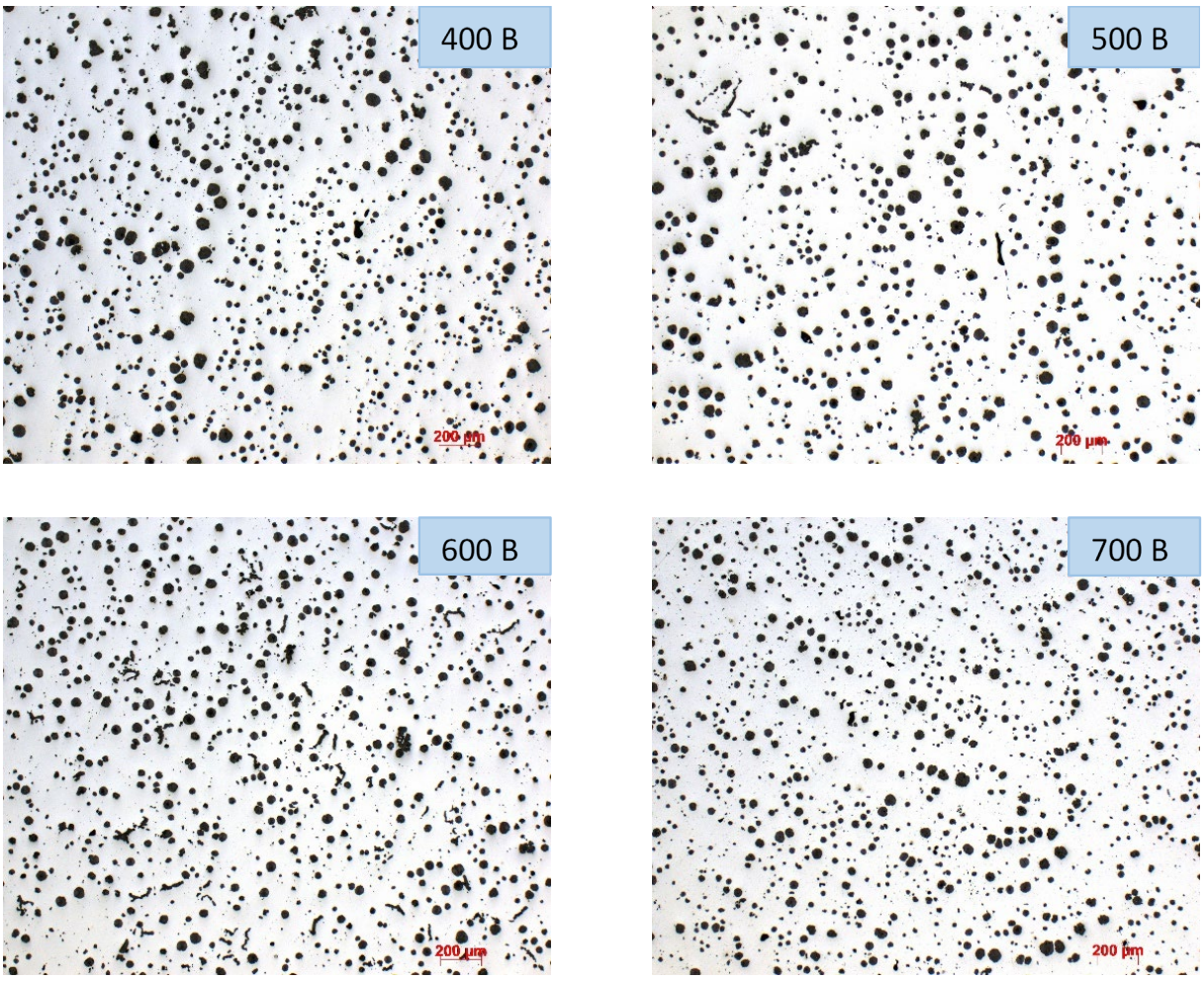

Figure 38 DCI series type B, non-etched. 50X

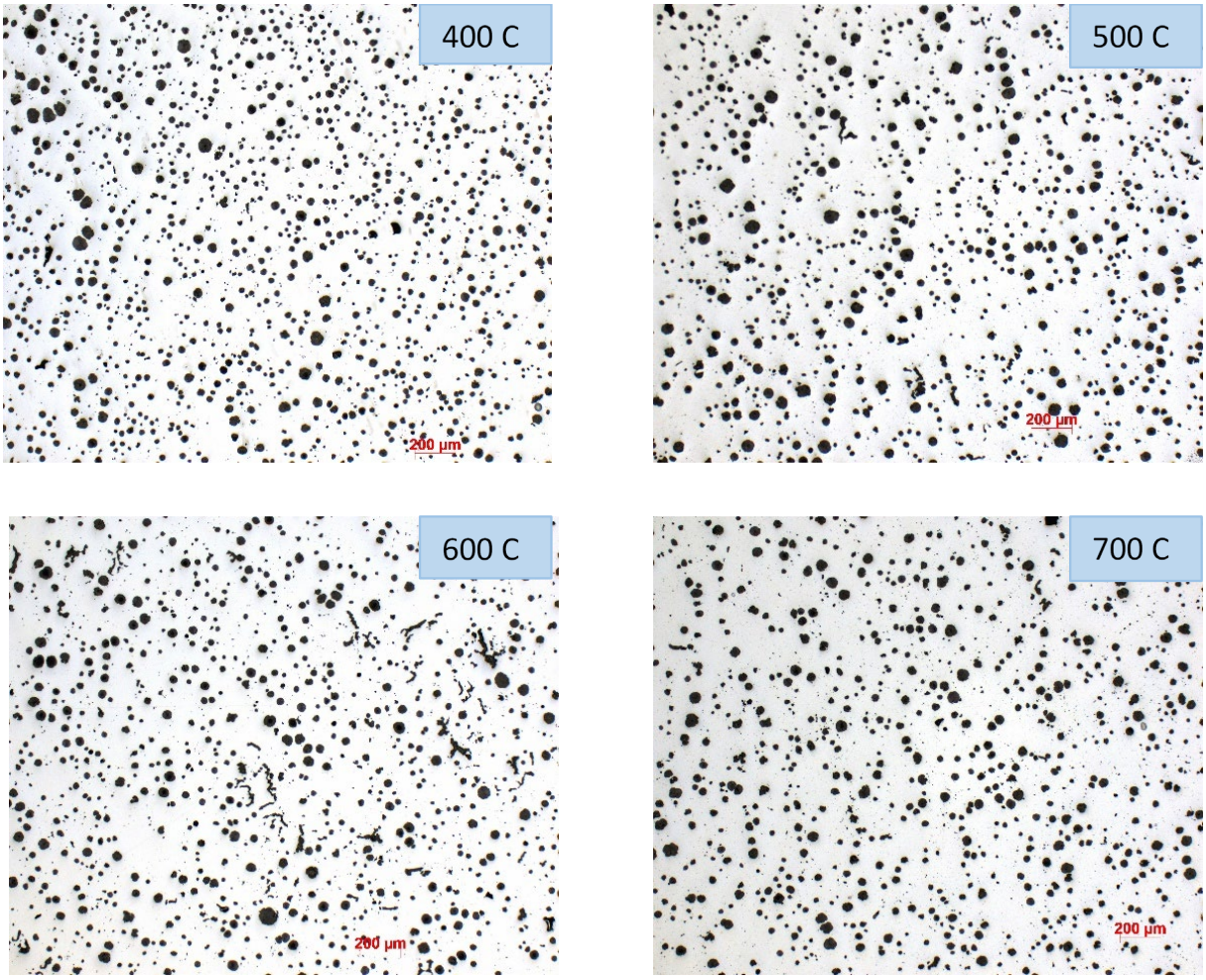

Figure 39 DCI series type C, non-etched. 50X

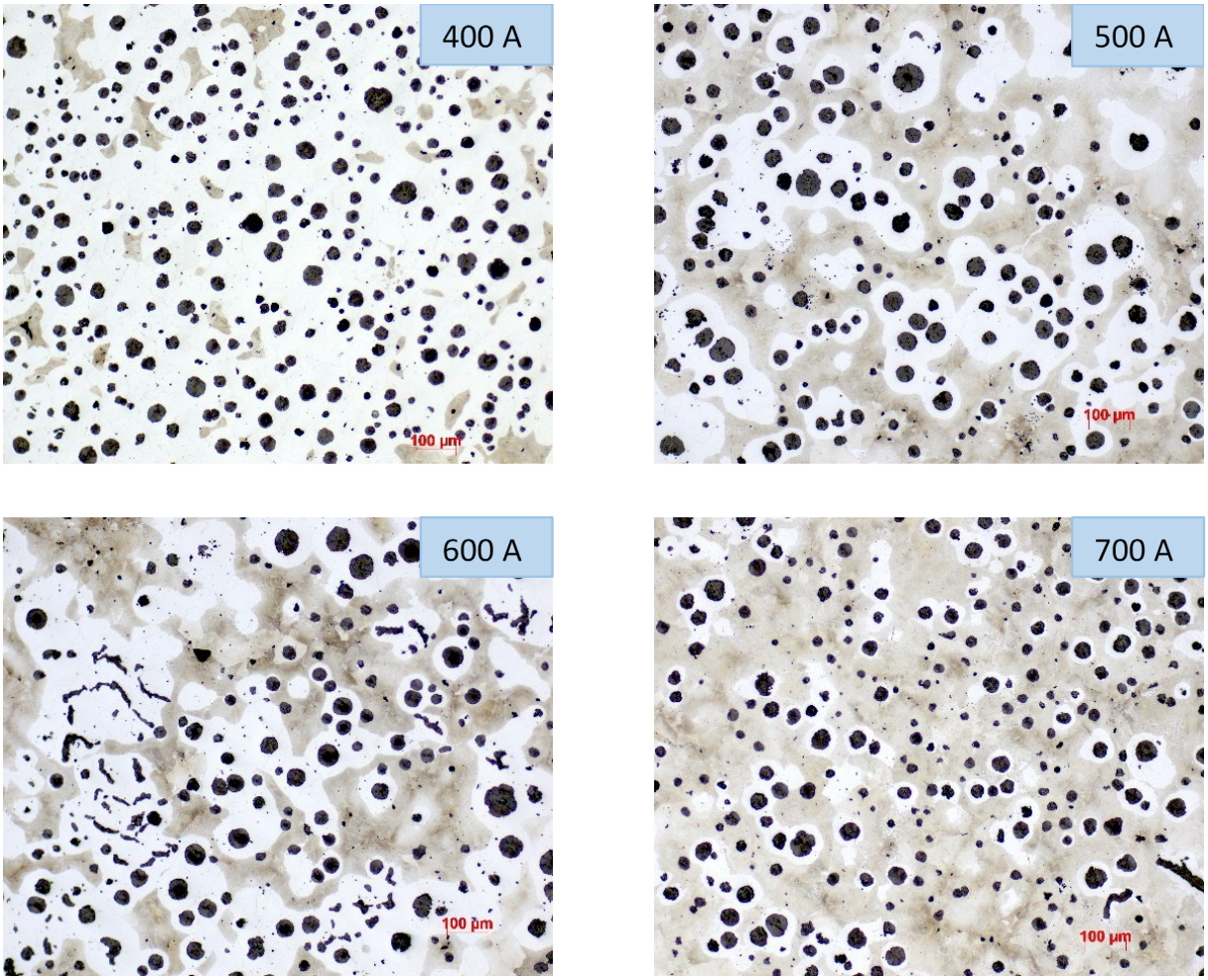

Figure 40 DCI series type A, etched with nital. 100X

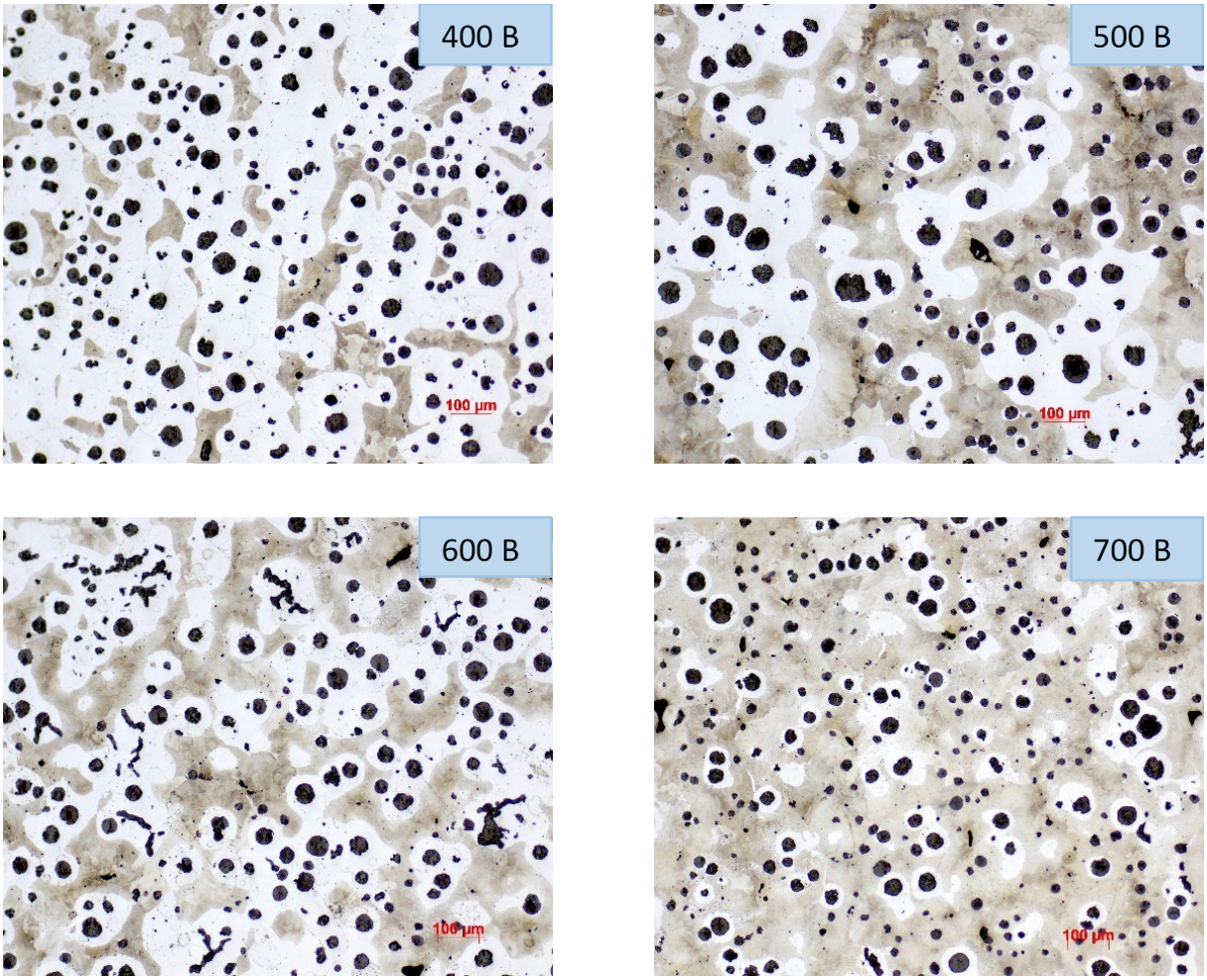

Figure 41 DCI series type B, etched with nital. 100X

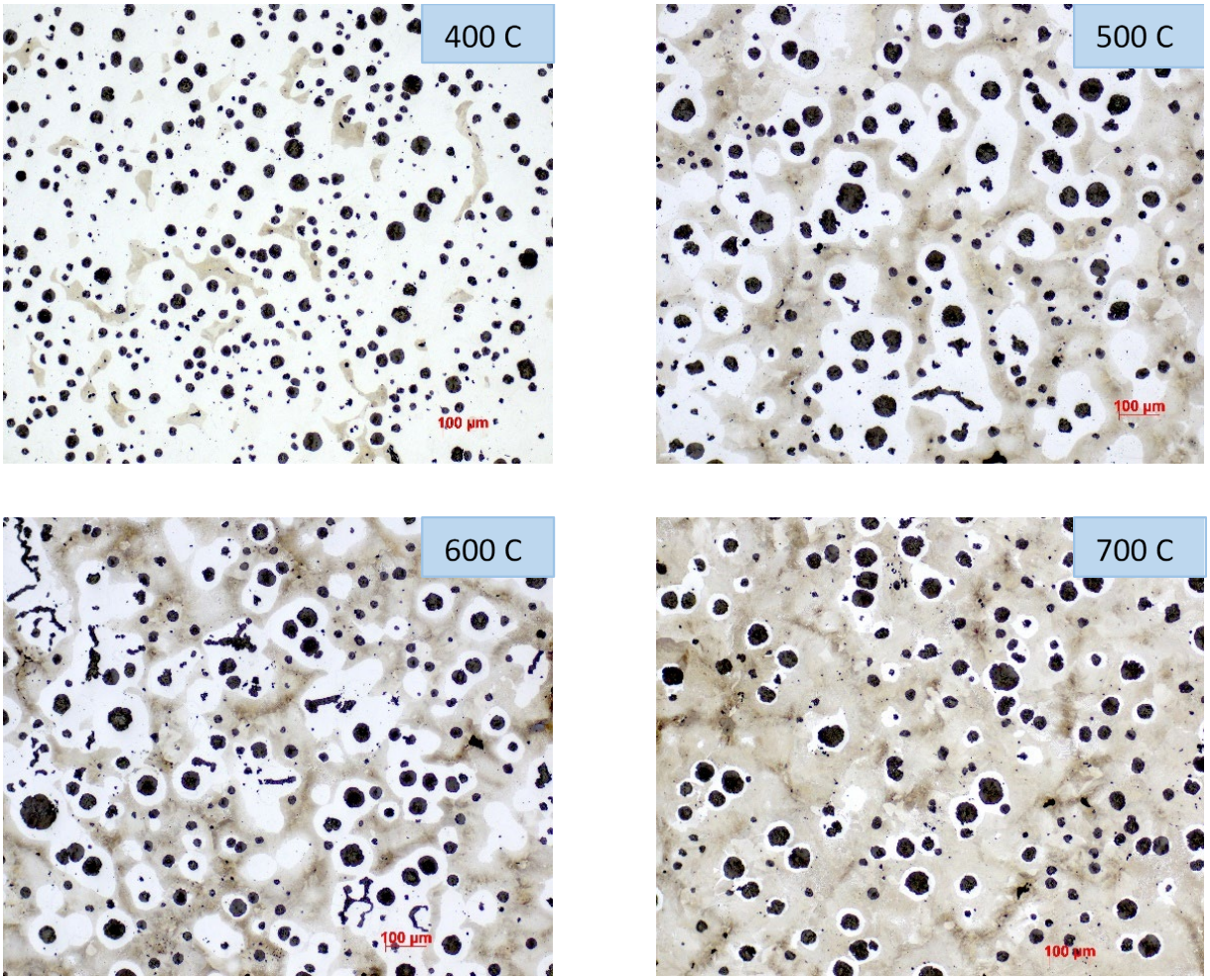

Figure 42 DCI series type C, etched with nital. 100X

APPENDIX C

It is important to consider that all the images in Appendix A were taken from random places within the central zones of the respective samples. They are overviews that can be used as references for the readers, so that further interpretations can be supported with the following graphite analysis. They were done using 10 micrographs along the whole cross section of the CT samples for each DCI in C samples only.

Figure 43 shows the shape distribution according to the standard ISO 945-1. The higher the shape number, the more round it is. As expected, graphite shapes have between 80-90% shape 5 (V) and 6 (VI), while 600 samples have about 20% concentration of vermicular-lamellar graphite.

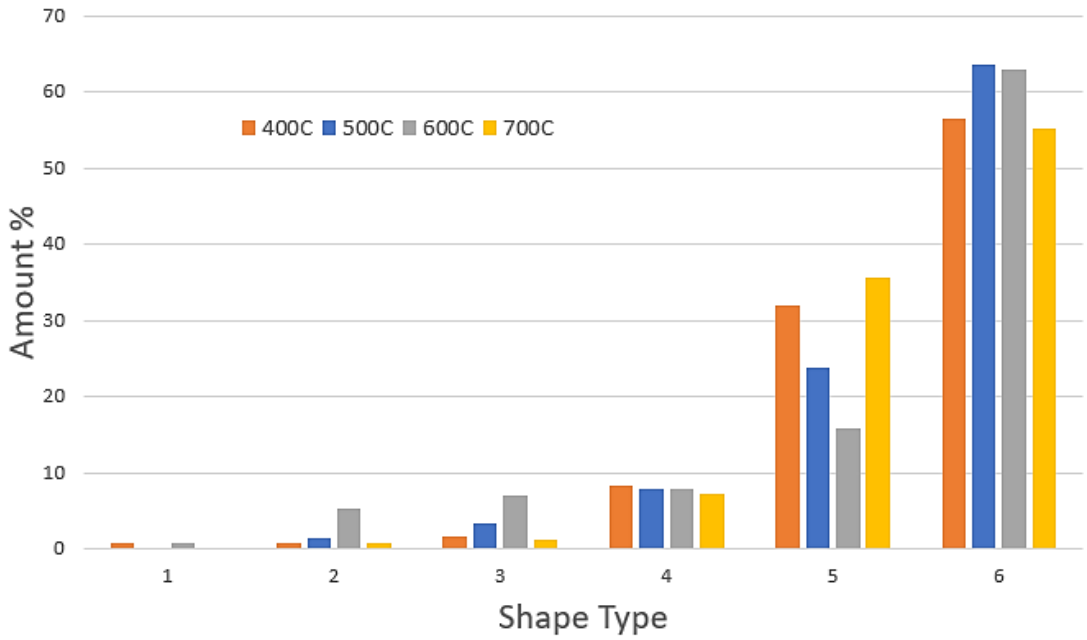

Figure 43 Graphite analysis: Shape distribution for each DCI

Figure 44 shows the size class distribution according to the same standard with the regarding size range aside. All materials have mostly class 6 graphite particles, following a Gaussian-like distribution towards the neighboring classes.

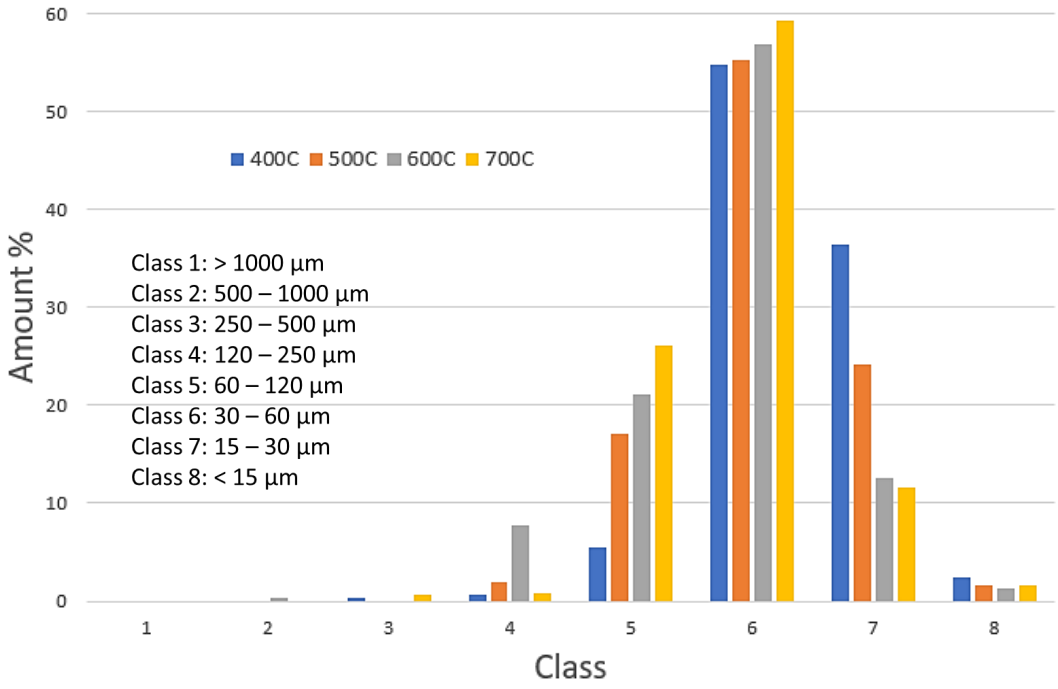

Figure 44 Graphite analysis: Size class distribution for each DCI

APPENDIX D

Due to the number of samples and tests done, only the most representative values were shown in the Results and Discussion sections. Therefore, Table 7 summarizes all the fatigue crack growth parameters at the threshold. Most of them were done at R=0,1 because, according to the *Materials Technology department of* SCANIA, it was the most common value at which their truck parts are subjected to.

Standard deviations σ are very low for ΔK_{th}, while for the effective values it increases due to the spread related to the crack closure phenomenon. Besides, all the samples tested under the same R were done at similar a/W ratios, which should also be considered for future studies and comparison.

Table 7 All relevant FCG parameters for each sample

Sample	R	ΔK_{th}	σ (ΔK_{th})	$\Delta K_{th,eff}$	σ ($\Delta K_{th,eff}$)	Kmax,th	σ (Kmax)	a/W
400A1 th1	***0,1***	***12,34***	***0,04***	***10,28***	***0,07***	***13,71***	***0,05***	***0,40***
400A1 th2	***0,1***	***12,87***	***0,02***	***12,65***	***0,26***	***14,31***	***0,02***	***0,49***
400B1 th1	***0,1***	***12,69***	***0,01***	***10,90***	***0,29***	***14,10***	***0,01***	***0,38***
400C2 th1	***0,1***	***13,09***	***0,00***	***10,35***	***0,12***	***14,54***	***0,00***	***0,39***
400A2 th1	***0,4***	***9,11***	***0,02***	***8,51***	***0,23***	***15,24***	***0,02***	***0,37***
400B2 th1	***0,4***	***9,47***	***0,04***	***7,76***	***1,66***	***15,78***	***0,06***	***0,37***
400C3 th1	***0,4***	***9,21***	***0,02***	***6,29***	***0,54***	***15,36***	***0,03***	***0,37***
400A2 th2	***0,7***	***5,96***	***0,01***	***5,96***	***0,01***	***19,87***	***0,03***	***0,53***
400C3 th2	***0,7***	***4,69***	***0,05***	***4,70***	***0,05***	***15,65***	***0,18***	***0,48***
500A1 th1	***0,1***	***12,46***	***0,05***	***11,36***	***0,06***	***13,84***	***0,05***	***0,39***
500A1 th2	***0,1***	***12,93***	***0,02***	***10,76***	***0,76***	***14,37***	***0,02***	***0,43***
500A2 th1	***0,1***	***12,88***	***0,01***	***9,66***	***0,01***	***14,32***	***0,01***	***0,39***
500B1 th1	***0,1***	***12,96***	***0,02***	***9,72***	***0,02***	***14,40***	***0,03***	***0,39***
500C2 th1	***0,1***	***11,83***	***0,01***	***9,32***	***0,22***	***13,15***	***0,01***	***0,42***
500B2 th1	***0,4***	***9,34***	***0,04***	***8,33***	***0,31***	***15,57***	***0,06***	***0,37***
500C3 th1	***0,4***	***8,92***	***0,01***	***7,49***	***0,65***	***14,87***	***0,02***	***0,40***
500A2 th3	***0,7***	***5,60***	***0,03***	***5,46***	***0,04***	***18,69***	***0,10***	***0,59***

500C3 th2	*0,7*	*4,67*	*0,03*	*4,65*	*0,03*	*15,59*	*0,10*	*0,53*
600A1 th1	*0,1*	*12,88*	*0,02*	*9,66*	*0,02*	*14,31*	*0,03*	*0,39*
600A1 th2	*0,1*	*13,44*	*0,03*	*11,31*	*0,23*	*14,94*	*0,03*	*0,47*
600A2 th1	*0,1*	*12,93*	*0,01*	*9,70*	*0,01*	*14,38*	*0,01*	*0,39*
600B1 th1	*0,1*	*12,53*	*0,01*	*10,15*	*1,07*	*13,92*	*0,01*	*0,40*
600C2 th1	*0,1*	*12,57*	*0,00*	*9,63*	*0,11*	*13,97*	*0,00*	*0,40*
600B2 th1	*0,4*	*9,67*	*0,02*	*8,74*	*0,22*	*16,13*	*0,03*	*0,36*
600C3 th1	*0,4*	*8,69*	*0,00*	*7,80*	*0,04*	*14,49*	*0,01*	*0,39*
600A2 th2	*0,7*	*5,70*	*0,02*	*5,66*	*0,03*	*19,00*	*0,08*	*0,54*
600C3 th2	*0,7*	*4,93*	*0,03*	*4,76*	*0,04*	*16,52*	*0,09*	*0,50*
700A1 th1	*0,1*	*11,94*	*0,01*	*8,94*	*0,05*	*13,27*	*0,02*	*0,41*
700A1 th2	*0,1*	*12,49*	*0,04*	*9,37*	*0,03*	*13,88*	*0,04*	*0,50*
700B1 th1	*0,1*	*12,21*	*0,02*	*9,52*	*0,44*	*13,57*	*0,02*	*0,41*
700C2 th1	*0,1*	*12,99*	*0,04*	*9,74*	*0,03*	*14,43*	*0,04*	*0,47*
700A2 th1	*0,4*	*8,72*	*0,02*	*7,07*	*0,17*	*14,55*	*0,03*	*0,40*
700B2 th1	*0,4*	*8,67*	*0,01*	*7,23*	*0,38*	*14,46*	*0,01*	*0,40*
700A2 th2	*0,7*	*5,21*	*0,03*	*4,99*	*0,07*	*17,33*	*0,10*	*0,59*
700B2 th2	*0,7*	*4,73*	*0,03*	*4,73*	*0,03*	*15,77*	*0,09*	*0,52*

In the same way Table 8 shows all the Paris Law parameters with their respective standard deviation σ for both n and C. The dimensions of C are given in mm/(lc×ΔK); with lc = load cycle. It is important to remind that there are significant differences in the dimensionless parameter m for samples tested at R=0,1, and all parameters they were obtained only through the K-decreasing method and the Paris region was not completely obtained.

Table 8 Paris Law parameters for all tested samples

Sample	R	m	σ (m)	C	σ (C)
400A1 th1	*0,1*	*6,3*	*0,3*	*4,5E-13*	*5,2E-13*
400A1 th2	*0,1*	*7,2*	*0,3*	*2,0E-14*	*2,1E-14*
400B1 th1	*0,1*	*3,5*	*1,1*	*7,4E-10*	*1,5E-08*
400C2 th1	*0,1*	*5,6*	*0,8*	*2,3E-12*	*1,9E-11*
400A2 th1	*0,4*	*3,9*	*0,3*	*8,9E-10*	*1,1E-09*
400B2 th1	*0,4*	*5,2*	*1,4*	*3,3E-11*	*8,5E-10*
400C3 th1	*0,4*	*4,4*	*0,3*	*2,1E-10*	*2,3E-10*
400A2 th2	*0,7*	*3,9*	*0,1*	*1,1E-09*	*1,9E-10*
400C3 th2	*0,7*	*4,3*	*0,1*	*6,5E-10*	*1,6E-10*
500A1 th1	*0,1*	*7,4*	*0,4*	*2,7E-14*	*5,1E-14*
500A1 th2	*0,1*	*5,7*	*1,5*	*2,2E-12*	*1,2E-10*
500A2 th1	*0,1*	*6,5*	*0,1*	*3,5E-13*	*1,7E-13*
500B1 th1	*0,1*	*6,8*	*0,3*	*1,6E-13*	*2,2E-13*
500C2 th1	*0,1*	*8,1*	*0,4*	*6,2E-15*	*1,1E-14*
500B2 th1	*0,4*	*4,9*	*0,3*	*9,3E-11*	*8,2E-11*
500C3 th1	*0,4*	*5,5*	*0,4*	*2,5E-11*	*4,7E-11*
500A2 th3	*0,7*	*4,4*	*0,1*	*4,4E-10*	*6,7E-11*
500C3 th2	*0,7*	*4,7*	*0,1*	*3,6E-10*	*6,9E-11*
600A1 th1	*0,1*	*6,0*	*0,4*	*1,3E-12*	*2,4E-12*
600A1 th2	*0,1*	*11,4*	*0,7*	*2,2E-19*	*1,5E-18*
600A2 th1	*0,1*	*4,9*	*0,3*	*3,0E-11*	*4,7E-11*
600B1 th1	*0,1*	*5,9*	*0,3*	*2,0E-12*	*2,6E-12*
600C2 th1	*0,1*	*5,7*	*0,1*	*3,7E-12*	*1,8E-12*

600B2 th1	***0,4***	***6,3***	***0,6***	***2,5E-12***	***9,5E-12***
600C3 th1	***0,4***	***5,7***	***0,4***	***1,7E-11***	***2,3E-11***
600A2 th2	***0,7***	***4,8***	***0,1***	***1,9E-10***	***2,9E-11***
600C3 th2	***0,7***	***4,8***	***0,1***	***2,5E-10***	***4,2E-11***
700A1 th1	***0,1***	***8,3***	***0,3***	***3,9E-15***	***5,9E-15***
700A1 th2	***0,1***	***6,0***	***0,3***	***9,9E-13***	***1,2E-12***
700B1 th1	***0,1***	***4,1***	***0,3***	***4,1E-10***	***4,8E-10***
700C2 th1	***0,1***	***5,8***	***0,8***	***2,7E-12***	***2,5E-11***
700A2 th1	***0,4***	***6,9***	***0,2***	***1,1E-12***	***7,2E-13***
700B2 th1	***0,4***	***5,2***	***0,2***	***6,6E-11***	***4,3E-11***
700A2 th2	***0,7***	***4,7***	***0,1***	***3,6E-10***	***4,8E-11***
700B2 th2	***0,7***	***4,7***	***0,1***	***4,0E-10***	***9,7E-11***